Article

Prenatal immune stress blunts microglia reactivity, impairing neurocircuitry

Lindsay N. Hayes[1], Kyongman An[2], Elisa Carloni[2], Fangze Li[2], Elizabeth Vincent[3], Chloë Trippaers[2,4], Manish Paranjpe[2], Gül Dölen[1], Loyal A. Goff[1,3], Adriana Ramos[1], Shin-ichi Kano[2,5] & Akira Sawa[1,2,3,6,7,8✉]

Recent studies suggested that microglia, the primary brain immune cells, can affect circuit connectivity and neuronal function[1,2]. Microglia infiltrate the neuroepithelium early in embryonic development and are maintained in the brain throughout adulthood[3,4]. Several maternal environmental factors—such as an aberrant microbiome, immune activation and poor nutrition—can influence prenatal brain development[5,6]. Nevertheless, it is unknown how changes in the prenatal environment instruct the developmental trajectory of infiltrating microglia, which in turn affect brain development and function. Here we show that, after maternal immune activation (MIA) in mice, microglia from the offspring have a long-lived decrease in immune reactivity (blunting) across the developmental trajectory. The blunted immune response was accompanied by changes in chromatin accessibility and reduced transcription factor occupancy of the open chromatin. Single-cell RNA-sequencing analysis revealed that MIA does not induce a distinct subpopulation but, rather, decreases the contribution to inflammatory microglia states. Prenatal replacement of microglia from MIA offspring with physiological infiltration of naive microglia ameliorated the immune blunting and restored a decrease in presynaptic vesicle release probability onto dopamine receptor type-two medium spiny neurons, indicating that aberrantly formed microglia due to an adverse prenatal environment affect the long-term microglia reactivity and proper striatal circuit development.

Microglia, the primary brain immune cells, have many functions across the lifespan. Their primary function is rapid immune activation to protect the brain, but dysfunction of microglia immune activation can result in poor outcomes for the surrounding neurons and glia[7,8]. As microglia are long-lived cells with early brain entry, aberrant microglia arriving in early development may have a key role in modulating these cell–cell interactions across the trajectory of health and disease. Several studies showed that prenatal stress has an effect on brain development and function in later life[9,10]. Nevertheless, the role and mechanism of microglia in the long-term changes elicited by prenatal stress are unclear.

Blunted microglia reactivity in adult MIA offspring

To address this knowledge gap, we tested whether a prenatal immune stressor (MIA) influenced microglia functions, including immune activation. To generate MIA offspring, we delivered an immune activator (polyinosinic:polycytidylic acid (PIC)) to pregnant dams at embryonic day 9.5 (E9.5) to target the first wave of microglia infiltrating the neuroepithelium[3]. To study how MIA influences the offspring immune response, we injected either a proinflammatory stimulus (lipopolysaccharide (LPS)) or saline (SAL) to adult offspring in vivo, isolated microglia and analysed the gene expression profiles (Extended Data Fig. 1). First, we compared gene expression between microglia from MIA offspring (MIA microglia) and those from control offspring (CON microglia). We observed only seven differentially expressed genes (DEGs) between MIA and CON microglia after SAL treatment (Fig. 1a and Extended Data Fig. 2). By contrast, we identified 401 DEGs between MIA and CON microglia after LPS treatment (Fig. 1a and Extended Data Fig. 2). Interestingly, the majority of the DEGs (76%) were downregulated in MIA compared with CON microglia (Fig. 1a). Furthermore, the DEGs showed significant negative enrichment for many immune response pathways (Fig. 1b). Together, adult immune reactivity is markedly reduced in MIA microglia, although the baseline (SAL) gene expression is similar between MIA and CON microglia.

To address the decreased MIA microglia immune reactivity directly, we compared the microglia gene expression between LPS and SAL treatment (LPS response genes). In CON microglia, 5,624 genes were differentially expressed between LPS and SAL treatment, whereas, in MIA microglia, fewer genes (4,284) were differentially expressed between LPS and SAL treatment (Fig. 1c and Extended Data Fig. 2).

[1]Solomon H. Snyder Department of Neuroscience, Johns Hopkins University School of Medicine, Baltimore, MD, USA. [2]Department of Psychiatry and Behavioral Sciences, Johns Hopkins University School of Medicine, Baltimore, MD, USA. [3]McKusick-Nathans Institute of Genetic Medicine, Johns Hopkins University School of Medicine, Baltimore, MD, USA. [4]Biomedical Research Institute, Hasselt University, Hasselt, Belgium. [5]Department of Psychiatry and Behavioral Neurobiology, University of Alabama at Birmingham Heersink School of Medicine, Birmingham, AL, USA. [6]Biomedical Engineering, Johns Hopkins University School of Medicine, Baltimore, MD, USA. [7]Pharmacology and Molecular Sciences, Johns Hopkins University School of Medicine, Baltimore, MD, USA. [8]Mental Health, Bloomberg School of Public Health, Johns Hopkins University School of Medicine, Baltimore, MD, USA. ✉e-mail: asawa1@jh.edu
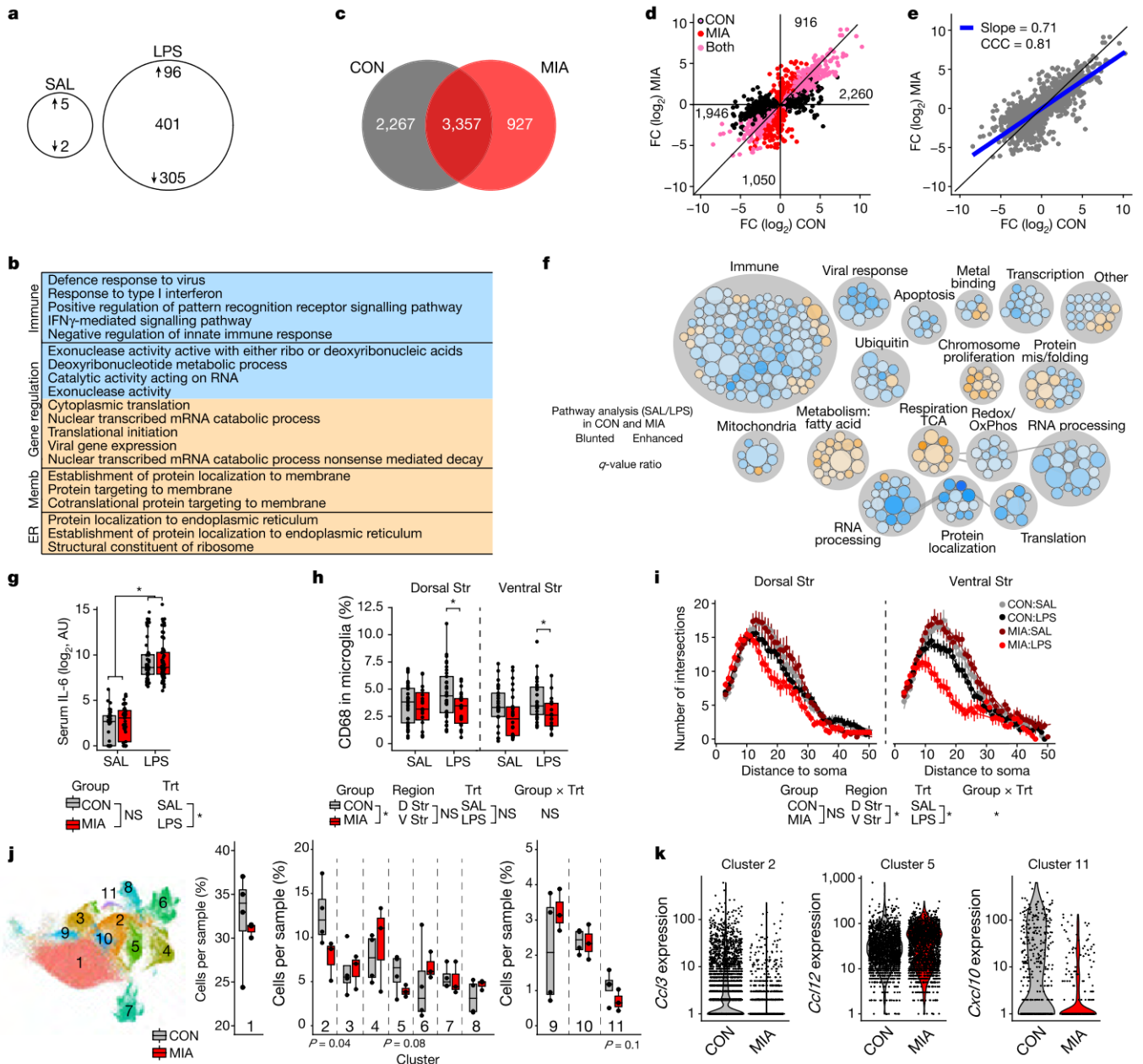
Fig. 1 | Diminished microglia immune response after MIA. a, DEGs ($q < 0.05$) between MIA and CON microglia after acute SAL or LPS treatment. **b**, The top 20 enriched gene sets from DEGs in **a** between MIA and CON microglia after acute LPS treatment. Reduction in MIA microglia (blue) and enhancement in MIA microglia (orange) are shown. ER, endoplasmic reticulum; memb, membrane. **c**, DEGs ($q < 0.05$) between SAL and LPS in CON microglia compared with MIA microglia. **d**,**e**, Plot (**d**) and linear regression (**e**) of the fold changes (FC; LPS/SAL) for the LPS-induced DEGs in both CON and MIA (pink), only CON (black) or only MIA (red) microglia. The numbers show DEGs for the LPS response in each section. The blue line shows a linear fit (slope = 0.71, CCC = 0.81). **f**, Comparison of the preranked gene set enrichment analysis for LPS-response genes between the CON and MIA microglia. Circles are Gene Ontology (GO) terms, and the colour indicates the magnitude of the q-value ratio ($q < 0.05$). Terms were selected with a $\log_2$-transformed q-value ratio of ≥1. Blunted LPS responses (blue) and enhanced LPS responses (orange) in MIA microglia are shown. OxPhos, oxidative phosphorylation. **g**, Serum IL-6 from CON and MIA offspring after SAL or LPS treatment. n values represent individual mice. Analysis was performed using a linear mixed-effect model, which showed an LPS effect, but no MIA effect. **h**, The percentage of CD68

inside microglia in the dorsal (D) and ventral (V) striatum (Str). n values represent individual cells. Statistical analysis was performed using three-way analysis of variance (ANOVA) (MIA, LPS, region) with emmeans post hoc test. We found a significant main effect of MIA with a significant emmeans post hoc test for MIA versus CON microglia after LPS treatment in both brain regions. **i**, The morphology of microglia using Sholl analysis. n values represent individual cells. Data are mean ± s.e.m. Analysis was performed using a linear mixed-effect model. There is a significant effect of treatment (Trt), brain region (region) and interaction between the MIA group and LPS treatment (group × Trt). **j**, Uniform manifold approximation and projection (UMAP) analysis of around 120,000 microglia grouped into 11 clusters. A differential abundance analysis is shown, quantifying the percentage of cells from each mouse to each cluster. n values represent individual mice. Statistical analysis was performed using a two-sided t-test. **k**, Gene expression ($\log_{10}$) for the distinct marker genes for clusters 2, 5 and 11 from CON and MIA microglia. n values represent individual cells. *$P < 0.05$. AU, arbitrary units. The box plots in **g**, **h** and **j** show the median (centre line), the interquartile range (IQR; box limits) and 1.5 × IQR (whiskers). Details of the statistical analyses are provided in Supplementary Table 1.

Specifically, 71% of the LPS-induced genes (2,260) showed diminished induction (decreased gene expression) in MIA microglia compared with CON microglia (Fig. 1d and Extended Data Fig. 2). Similarly, 65% of the LPS-suppressed genes (1,946) showed diminished suppression (increased gene expression) in MIA compared with CON microglia (Fig. 1d and Extended Data Fig. 2). Together, these results indicate a blunted immune response in MIA microglia compared with CON microglia, where a blunted gene is defined as any gene with a smaller absolute fold change in its LPS response in MIA microglia compared with CON microglia. We also demonstrated the immune blunting by fitting a regression line to the fold change values comparing the LPS response between CON and MIA microglia with a slope of about 0.7 and a concordance coefficient of around 0.8, both less than 1 (Fig. 1e and Extended Data Fig. 2). These data are in contrast to the expectation of a hyperactive immune response in MIA[5,11].

To functionally characterize this result, we compared two independent gene set enrichment analyses to identify specific molecular pathways that were differentially enriched between MIA and CON microglia in the context of their response to in vivo LPS treatment in adulthood. We found a strong decrease in the innate immune response pathways, including interferon signalling in MIA microglia (Fig. 1f). Moreover, we found an enhancement in the tricarboxylic acid cycle and fatty acid metabolism in parallel with a reduction in oxidative phosphorylation, redox pathways, electron transport chain and respiratory pathways in MIA microglia (Fig. 1f). The imbalance of the mitochondrial pathways observed in MIA microglia suggests an impaired immunometabolic response. Together, these results emphasize broad functional adaptations that are implemented in microglia in response to a change in the maternal microenvironment.

We next addressed whether there is a regional specificity of the blunted LPS response in adult MIA microglia. We found that MIA microglia from the frontal cortex and striatum both showed a blunted immune response compared with CON microglia, but the striatum showed a more robust effect than the frontal cortex (Extended Data Fig. 3a,b). To determine the specificity of the immune blunting to MIA microglia, rather than a bias in the data, we compared the LPS response between microglia from the frontal cortex and those from the striatum (mixing both CON and MIA together) and found a more concordant immune response (slope = 0.9, concordance coefficient (CCC) = 0.9) indicating that the blunted immune response is specific to MIA microglia (Extended Data Fig. 3c–e). Furthermore, the peripheral immune response to LPS treatment between MIA and CON offspring was not different as measured by serum interleukin-6 (IL-6), indicating that the peripheral immune response was normal (Fig. 1g). Together, the diminished immune responsiveness is a specific feature associated with MIA microglia in the brain.

Next, we functionally validated these in vivo observations in adult offspring using histology (Fig. 1h,i and Extended Data Fig. 4). We measured the density, morphology and lysosomal content of adult microglia in the dorsal and ventral striatum (Fig. 1h,i and Extended Data Fig. 4) because the striatal microglia showed a stronger immune phenotype (Extended Data Fig. 3a,b). Consistent with a blunted immune reactivity, we found that MIA microglia had less CD68+ lysosomes compared with CON microglia after in vivo LPS treatment (Fig. 1h and Extended Data Fig. 4b–d). Furthermore, MIA microglia were significantly smaller than CON microglia after LPS treatment, although morphological differences were negligible after SAL treatment, indicating an impaired responsiveness in MIA microglia (Fig. 1i and Extended Data Fig. 4a). The microglia density was unchanged after both SAL and LPS treatments (Extended Data Fig. 4e). Together, these data support a blunted immune response phenotype in MIA microglia by histology.

Several single-cell RNA-sequencing (RNA-seq) studies identified unique microglia subpopulations, particularly in neurodegenerative conditions[12–16]. We therefore evaluated whether the blunted immune response phenotype occurs in a distinct subset of microglia.

Among all of the LPS treated cells, we identified 11 distinct clusters of microglia, but no distinct cluster for MIA microglia compared with CON microglia (Fig. 1j,k and Extended Data Fig. 5a–c). We next performed an abundance assay to quantify the proportion of cells from each sample to each cluster. We found that MIA had a reduced abundance in the pro-inflammatory cluster 2 (Ccl3+), and a decreasing trend in clusters 5 (Ccl12+) and 11 (interferon cluster, Ifit2+ Cxcl10+) (Fig. 1j,k and Extended Data Fig. 5). These data indicate that MIA affects some proinflammatory clusters, consistent with the idea of a blunted immune phenotype in MIA microglia observed in the bulk RNA-seq analysis.

Blunted MIA microglia reactivity in development

We next addressed the immune responsiveness of microglia in the developmental course after MIA by extracting microglia from the striatum and cortex of both MIA and CON offspring and culturing the primary microglia in vitro. This enabled us to characterize the immune responsiveness of embryonic microglia and to obtain complementary findings with the in vivo data. We stimulated the extracted microglia with LPS in vitro and quantified the secretion of the cytokines IL-6 and TNFα from the microglia into the culture medium. Consistent with the in vivo data, we found that adult microglia from the striatum of MIA offspring showed a reduction in secreted proinflammatory cytokines compared with CON microglia (Fig. 2a). Importantly, a similar diminished immune response was observed at E18 in MIA compared with CON microglia from the striatum, indicating a long-lived immune-blunting phenotype (Fig. 2a). In cortical microglia, MIA showed a mild decrease in immune response in adulthood and no significant change at E18, indicating that the cortex has a delayed and milder immune-blunting phenotype potentially due to the later maturation of cortical development compared with the striatum (Fig. 2b). These in vitro data suggest that a prenatal immune stressor induced a long-lived blunting in MIA microglia activation to a subsequent immune stimulus, consistent with the blunted response of microglia to in vivo stimulation in adulthood.

The neonatal brain contains endogenous stressors that can induce microglia to become reactive[15,17,18]. Thus, by directly examining in vivo microglia from freshly extracted neonatal brains, we can evaluate the responsivity of MIA microglia to intrinsic activators. We found 2,034 DEGs between neonatal MIA and CON microglia (Fig. 2c–e). Similar to LPS-activated microglia in adulthood (Fig. 1b,f), these DEGs between neonatal MIA and CON microglia showed a reduction in pathways associated with immune response, phagocytosis, RNA processing and protein localization (Fig. 2d,e). Moreover, 123 of these DEGs were commonly changed (false-discovery rate (FDR) < 0.1) in neonatal (intrinsically activated) microglia and adult LPS-treated microglia (Fig. 2f). Most of the genes were downregulated in neonatal microglia (88 genes) and in adult LPS-treated microglia (75 genes) (Fig. 2f). These genes were functionally related to the innate immune response and were enriched for target genes of the interferon pathway (IRF1, IRF2, IRF7 and IRF8)[19] (Fig. 2f). Together, MIA results in a diminished microglial reactivity to both intrinsic activation in the neonatal stage and exogenous activation by LPS in adulthood, with an impairment in overlapping functional pathways.

We also determined whether the DEGs between MIA and CON across datasets were enriched for disease-associated risk genes by examining datasets from genome-wide association studies (GWAS)[20]. We found that DEGs between MIA and CON were enriched for schizophrenia-risk genes more than risk genes for autism spectrum disorder, attention deficit hyperactivity disorder, bipolar disorder and major depressive disorder (Fig. 2g). Schizophrenia is a syndrome of neurodevelopmental origin with symptom onset after adolescence in contrast to child-onset developmental conditions, such as autism spectrum disorder and attention deficit hyperactivity disorder, or adult-onset conditions, such
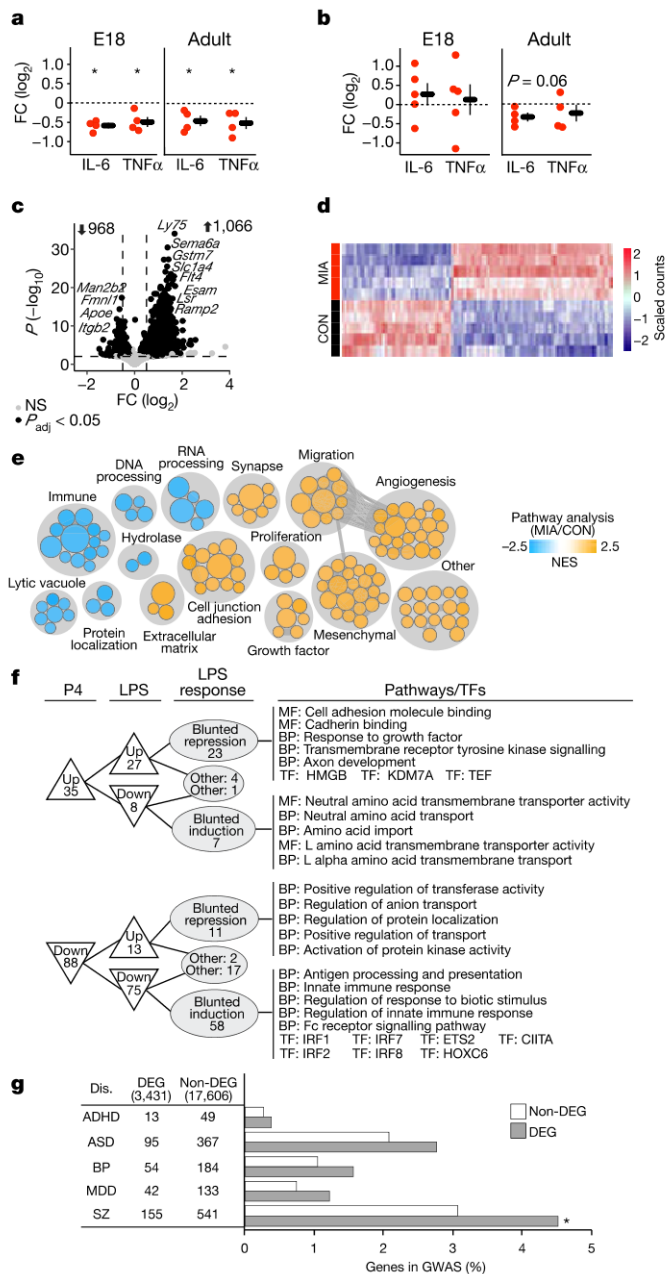
Fig. 2 | Diminished microglia reactivity in development after MIA.
a,**b**, Quantification of secreted IL-6 and tumour necrosis factor alpha (TNFα) from LPS-stimulated microglia in vitro at E18 and adulthood from the whole striatum (**a**) and cortex (Ctx) (**b**). Data are mean ± s.e.m. with each experiment normalized to CON. Statistical analysis was performed using a one-sample t-test. n values represent independent culture experiments. E18: $n = 4$ (Str, IL-6), $n = 4$ (Str, TNFα), $n = 5$ (Ctx, IL-6) and $n = 5$ (Ctx, TNFα) litters; adult: $n = 4$ (all groups) cultures, each with 2 mice pooled from 3 litters for both CON and MIA. $t_3 = -8.1$, $P = 0.004$ (E18, Str, IL-6); $t_3 = -3.8$, $P = 0.032$ (E18, Str, TNFα); $t_3 = -3.3$, $P = 0.046$ (adult, Str, IL-6); $t_3 = -3.2$, $P = 0.048$ (adult, Str, TNFα); $t_4 = 0.939$, $P = 0.40$ (E18, Ctx, IL-6); $t_4 = 0.32$, $P = 0.77$ (E18, Ctx, TNFα); $t_3 = -2.9$, $P = 0.06$ (adult, Ctx, IL-6); $t_3 = -1.1$, $P = 0.35$ (adult, Ctx, TNFα). **c**, Volcano plot of the DEGs at postnatal day 4 (P4) between MIA and CON microglia from the whole neonatal brain (black dots indicate multiple-comparison adjusted $P < 0.05$ (P_{adj}) using DESeq2. **d**, Heat map of neonatal DEGs between MIA and CON microglia at P4. **e**, Gene set enrichment analysis of the DEGs in **c** with blue pathways diminished in MIA microglia and orange pathways enhanced in MIA microglia. NES, normalized enrichment score. **f**, The 123 overlapping DEGs ($q < 0.1$) between MIA and CON from neonatal microglia and LPS-treated adult microglia along with enriched pathways (molecular function (MF) and biological process (BP)) and transcription factor (TF) regulators. **g**, Enrichment of GWAS risk genes for neuropsychiatric disorders (dis.) among DEGs between MIA and CON microglia. $P < 0.05$, determined using χ^2 tests with Bonferroni correction. Data are counts and percentage of GWAS risk genes among the DEG or non-DEGs. Attention deficit hyperactivity disorder (ADHD), autism spectrum disorder (ASD), bipolar disorder (BP), major depressive disorder (MDD) and schizophrenia (SZ). *$P < 0.05$. Details of the statistical analyses are provided in Supplementary Table 1.

accessible regions (DARs) were more open in MIA microglia compared with CON microglia (Fig. 3a). After correction for multiple comparisons, we identified 113 more open DARs, approximately a quarter of which were near transcriptional start sites (Fig. 3b). We used the Genomic Regions Enrichment of Annotations Tool to identify enriched pathways for the open chromatin regions, including the aforementioned immune regulation, lysosomal and protein modification pathways (Fig. 3c). However, a remaining question is how a more open chromatin structure could lead to a blunted transcriptional program.

To address this question, we used transcription factor foot-printing analysis to quantitatively evaluate the occupancy of transcription factors to the open chromatin regions by identifying smaller regions (10–20 base pairs) of occupied chromatin within the broader open chromatin regions (200–500 base pairs) and identifying the matching transcription factor motifs[23,24]. We followed the strategy from established studies that examined how transcriptional gene expression is regulated by transcription factors through this analysis based on chromatin accessibility data[25–27]. We identified 83 transcription factors with differential occupancy between MIA and CON microglia with 76% showing less occupancy in MIA microglia compared with CON microglia, including GATA4, SMAD3 and STAT1 (Fig. 3d), which are important transcription factors that regulate the immune response, particularly the interferon response[28–30]. There is a precedence from previous studies that showed a nonlinear relationship between open chromatin and transcription factor occupancy in other biological systems[31–33]. To confirm the ATAC transcription factor occupancy results indicating impaired interferon signalling, we found that the *Stat1* gene and several STAT1-target genes (*B2m*, *Il1b*, *Irf1* and *Myd88*) consistently showed reduced gene expression in MIA microglia after LPS treatment (Fig. 3e). We next performed a network analysis of the paired ATAC–seq and RNA-seq data together to identify transcription factors and target networks that are enriched in CON or MIA microglia after LPS treatment (Extended Data Fig 6). We found more repressive networks in MIA microglia and more activator networks in CON microglia (Extended Data Fig 6a). Specifically, there was enhanced transcription

as bipolar disorder and major depressive disorder[21,22]. As a result, the contribution of immune mechanisms to autism may precede schizophrenia across the developmental trajectory. Thus, the pathological involvement of microglia throughout the developmental trajectory may be important for schizophrenia. In summary, these data provide evidence for a common underlying pathophysiology between environmental stressors (that is, MIA) and genetic risk factors on microglia biology in disease.

Epigenetic mechanism of MIA microglia blunting

Next, we examined how MIA could induce the blunted immune phenotype in adulthood. We hypothesized that the long-term impairment might be associated with an epigenetic change that interfered with transcriptional regulation of immune activation. To test this idea, we performed an assay for transposase accessible chromatin with sequencing (ATAC–seq) analysis of adult MIA and CON microglia after LPS treatment. Notably, we found that 97% of the differentially
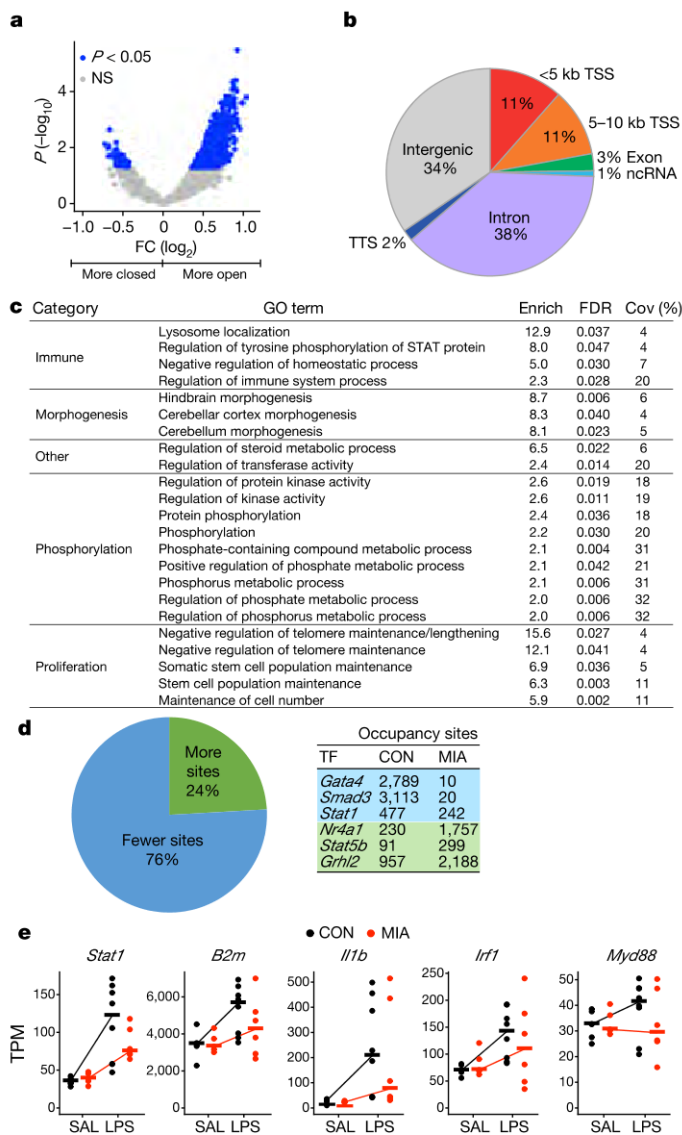
Fig. 3 | Epigenetic reprogramming and transcriptional regulation of MIA microglia. a, Volcano plot of DARs of ATAC–seq between MIA and CON microglia from the whole striatum after LPS treatment. Blue dots show unadjusted $P < 0.05$ using DiffBind. A positive fold change indicates more open chromatin in MIA microglia, and a negative fold change indicates more closed chromatin in MIA microglia. **b**, The spatial location of 113 DARs after a permutation test (multiple comparison adjusted $P < 0.05$) with the location respective to the transcriptional start site (TSS), exon, non-coding RNA (ncRNA), intron, intergenic and transcriptional termination site (TTS). **c**, Pathway analysis using GREAT for the 113 DARs between MIA and CON microglia after LPS treatment. Twenty-three enriched GO pathways with FDR < 0.05. Enrichment score (enrich) and coverage (cov). **d**, Differential transcription factor occupancy sites in the open chromatin regions of MIA and CON microglia after LPS treatment. Transcription factors were included with more than 250 total sites and ≥0.5 $\log_2$-transformed fold change. The right table indicates the top 3 more and less occupied transcription factors with the number of occupancy sites in CON and MIA microglia after LPS. **e**, Gene expression (transcripts per million, TPM) of CON and MIA microglia after SAL or LPS treatment for *Stat1* and STAT1-target genes (*B2m*, *Il1b*, *Irf1* and *Myd88*). Data are mean. *n* values represent individual mice. *n* = 6 mice from 5 litters (CON, SAL), *n* = 8 mice from 7 litters (CON, LPS), *n* = 5 mice from 3 litters (MIA, SAL) and *n* = 6 mice from 5 litters (MIA, LPS). Details of the statistical analyses are provided Supplementary Table 1.

factor–target interactions in the interferon pathway, including IRF1, IRF2, STAT1 and STAT2, in CON microglia after LPS treatment compared with MIA microglia (Extended Data Fig 6b,c). Finally, we performed an experimental validation using CUT&RUN–quantitative PCR (qPCR) with transcription factor capture antibodies against IRF1 and STAT2[34,35]. We found there was a trend towards less total DNA pulled-down by STAT2 and IRF1 in MIA microglia after acute LPS treatment (Extended Data Fig 6d,e). Furthermore, there was less capture of specific target DNA for the transcription factor–targets IRF1–*Fas*, IRF1–*Il6* and STAT2–*Il23* (Extended Data Fig 6f,g). Together, these data indicate that the chromatin is more open in adult MIA microglia compared with CON microglia after LPS treatment, and there are fewer transcription factors occupying these open regions, which results in blunted immune response gene activation at the molecular level.

Rescue of MIA microglia by prenatal replacement

We next tested whether long-term microglia impairment may be ameliorated by ablating the MIA-impaired microglia to enable naive microglia to reinfiltrate the developmental brain after the MIA stressor. To accomplish the prenatal microglia replacement, we treated pregnant dams with a CSF1R antagonist (PLX5622) between E9.5 and E12.5 to effectively eliminate embryonic myeloid cells (Extended Data Fig. 7). The short treatment of the CSF1R antagonist did not affect the MIA maternal immune response as measured by serum IL-6 protein expression (Extended Data Fig. 7f). In adulthood, we compared gene expression changes in response to LPS (LPS-response genes) among CON microglia, MIA microglia, repopulated microglia in MIA (repopulated MIA microglia) and repopulated microglia in CON (repopulated CON microglia). We found that the LPS response in the repopulated MIA microglia showed an amelioration of the blunted immune response by gene expression (Fig. 4a–g and Extended Data Fig. 8). MIA microglia, repopulated MIA microglia and repopulated CON microglia showed slopes for fold change linear regression of 0.74, 0.86 and 0.90, respectively, indicating that the LPS response of the repopulated MIA microglia is more similar to the LPS response of CON microglia (0.9) than that of MIA microglia (0.7) (Fig. 4a–g).

The amelioration of the blunted immune response in repopulated MIA microglia was also addressed at the single-cell level (Fig. 4h–j and Extended Data Fig. 5). We found the repopulated MIA microglia did not cluster distinctly from the healthy CON microglia (Extended Data Fig. 5c). Furthermore, the abundance assay to quantify the proportion of cells from each sample to each cluster found that the repopulated MIA microglia showed a rescued contribution to cluster 2 (*Ccl3*+) and cluster 5 (*Ccl12*+) (Fig. 4h–j). However, cluster 11 (interferon cluster, *Ifit2*+*Cxcl10*+) still showed a small reduction in the repopulated MIA microglia (Fig. 4i–j). These data indicate that the repopulated cells are indistinguishable from CON (endogenous) microglia, and the repopulated MIA microglia ameliorated the reduced contribution to the proinflammatory clusters.

The amelioration of the blunted immune response in the repopulated MIA microglia was confirmed at the protein level using IL-1β, TNFα and IL-6 (Fig. 4k–m). After LPS treatment, adult MIA microglia showed reduced protein expression of TNFα, a trend towards decreased IL-1β, but no change in IL-6, whereas the repopulated MIA microglia did not show such deficits (Fig. 4k–m). These protein data are consistent with the transcriptional data, in which the blunted MIA microglia are rescued by prenatal microglia replacement.

Effect of MIA microglia on astrocytes and neurons

To evaluate the cell non-autonomous effects of MIA microglia on the surrounding glia and neurons, we evaluated cytokine protein expression of the astrocytes and non-microglial/non-astrocytic (negative) cells after LPS treatment. In contrast to the reduced protein expression in MIA
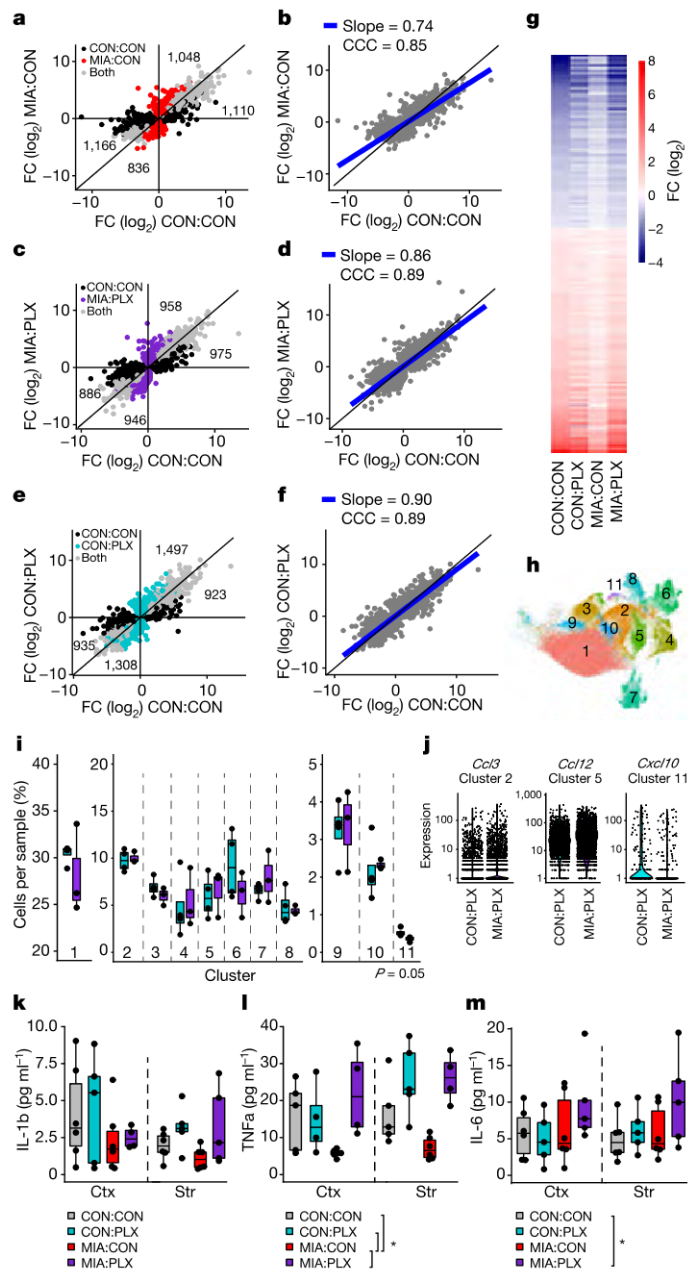
Fig. 4 | Amelioration of microglia blunting after prenatal replacement.
a,**b**, Plot (**a**) and linear regression (**b**) of the fold change for the LPS-induced DEGs in both CON mice with control treatment (CON:CON) and MIA mice with control treatment (MIA:CON) (grey), only CON:CON (black) or only MIA:CON microglia (red). The numbers indicate the total number of LPS-response genes in **a**, **c** and **e**. The blue line is a linear fit (slope = 0.74 and CCC = 0.85). **c**,**d**, Plot (**c**) and linear regression (**d**) of the fold change for the LPS-induced DEGs in both CON:CON and MIA mice with PLX treatment (MIA:PLX) (grey), only CON:CON (black) or only MIA:PLX microglia (purple). The blue line is the linear fit (slope = 0.86 and CCC = 0.89). **e**,**f**, Plot (**e**) and linear regression (**f**) of the fold change for the LPS-induced DEGs in both CON:CON and CON mice with PLX treatment (CON:PLX) (grey), only CON:CON (black) or only CON:PLX microglia (cyan). The blue line is the linear fit (slope = 0.90 and CCC = 0.89). **g**, Heat map of the log$_2$-transformed fold change for LPS-response genes in CON:CON, CON:PLX, MIA:CON and MIA:PLX. **h**, UMAP analysis of approximately 120,000 microglia grouped into 11 clusters. **i**, Differential abundance analysis quantifying the percentage of cells from each sample in each cluster. n values represent individual mice. Statistical analysis was performed using a two-sided t-test. $n = 4$ (CON:PLX), $n = 3$ (MIA:PLX). **j**, Gene expression (log$_{10}$) for the distinct marker genes for clusters 2, 5 and 11 in CON and MIA microglia after prenatal replacement. **k**–**m**, Protein expression of the cytokines IL-1β (**k**), TNFα (**l**) and IL-6 (**m**) in microglia from the CON:CON (grey), CON:PLX (cyan), MIA:CON (red) and MIA:PLX (purple) groups. n values represent individual samples from pooled mice. Statistical analysis was performed using two-way ANOVA with Tukey post hoc test. *$P < 0.05$. The box plots in **i** and **k**–**m** show the median (centre line), the IQR (box limits) and 1.5 × IQR (whiskers). Details of the statistical analyses are provided in Supplementary Table 1.

and Extended Data Fig. 9a). The sEPSC amplitude was unchanged in both types of MSNs (Extended Data Fig. 9b). We found no change in the spine density of MSNs of the ventral striatum (Extended Data Fig. 9c). However, we found an increase in the paired pulse ratio of D2R MSNs, but not D1R MSNs (Fig. 5d), suggesting a decrease in the presynaptic probability of vesicle release onto D2R MSNs in adult MIA offspring. To ensure that the decreased presynaptic release probability was independent of presynaptic cell excitability, we measured miniature EPSCs (mEPSCs) in D2R MSNs and found a decrease in the frequency, without any change in the amplitude (Fig. 5e and Extended Data Fig. 9d).

Finally, we aimed to determine whether the reduced connectivity of D2R MSNs was causally related to MIA microglia during the developmental trajectory. To address this question, we performed mEPSC recordings in CON and MIA offspring after prenatal microglia replacement. We found that the reduced mEPSC frequency in MIA offspring was rescued to the control levels after prenatal microglia replacement with no change in amplitude (Fig. 5f). Moreover, the microglia replacement alone did not alter the physiological properties of the D2R MSNs in the CON offspring (Fig. 5f). These results imply that MIA microglia causally underlie the dysfunctional connectivity of the ventral striatal circuit with a decrease in the glutamatergic presynaptic release probability specifically onto D2R MSNs.

Discussion

Here we address a fundamental biological question of how infiltrating microglia during early brain development are affected by their prenatal environment that may influence neuronal network formation. We demonstrated that prenatal immune stress diminishes microglia reactivity, which results in functional impairment of activation to subsequent stressors. The microglia dysfunction may be masked at baseline, but is revealed when microglia are needed to respond to either intrinsic (neonatal) or extrinsic (LPS) stimuli. We propose a new working model in which prenatal immune stress acts as a tolerizing stimulus leading to a change in the chromatin structure, transcription factor occupancy and transcriptional regulation of gene expression. Moreover, our data

microglia (Fig. 4k–m), astrocytes and non-microglial/non-astrocytic (negative) cells showed increased expression of IL-6 in MIA, indicating that astrocytes have an enhanced immune response (Fig. 5a,b). IL-1β and TNFα were undetectable in the astrocytes and negative cells after LPS treatment. Prenatal microglia replacement normalized the pathological change of astrocytes (Fig. 5a,b), indicating that impaired microglia reactivity probably underlies the changes in astrocytes of MIA offspring.

To evaluate the cell non-autonomous effect of MIA microglia on brain development and neuronal function, we evaluated the function of medium spiny neurons (MSNs) in the ventral striatum of adult MIA offspring by electrophysiological recordings. Dopamine dysfunction was previously identified in MIA and the striatum is a major target of the dopamine neuron circuitry[1,36] but, to our knowledge, no study has addressed MSN dysfunction in MIA offspring at the electrophysiological level. We found a decreased frequency of the spontaneous excitatory postsynaptic current (sEPSC) in dopamine receptor type-2 (D2R) MSNs, but not in dopamine receptor type 1 (D1R) MSNs (Fig. 5c

state of astrocytes in adult MIA offspring. Thus, our data emphasize the importance of evaluating cells in addition to microglia as a source of immune molecules in disease.

An outstanding question for future studies is to carefully address the effect of sex on microglia functional deficits as male and female microglia show different immune responsiveness[40,41] and developmental and psychiatric disorders also show sex differences[42]. Although we show some cursory evidence that the blunting phenotype is more robust in males (Extended Data Fig. 10a–d), this needs to be explored in greater detail in future studies. Another interesting extension is on the specificity of the D2R MSN physiological change in MIA in the ventral striatum. A recent study showed the critical role of microglia in regulating D1R MSN circuit development[2] and we expect that similar mechanisms are probably involved in the D2R MSN circuitry. Finally, further research is required to investigate the microglia states induced by LPS including the functional roles, temporal regulation and spatial allocation of these activation states.

Online content

Any methods, additional references, Nature Research reporting summaries, source data, extended data, supplementary information, acknowledgements, peer review information; details of author contributions and competing interests; and statements of data and code availability are available at https://doi.org/10.1038/s41586-022-05274-z.

1. Squarzoni, P. et al. Microglia modulate wiring of the embryonic forebrain. Cell Rep. 8, 1271–1279 (2014).
2. Badimon, A. et al. Negative feedback control of neuronal activity by microglia. Nature 586, 417–423 (2020).
3. Ginhoux, F. et al. Fate mapping analysis reveals that adult microglia derive from primitive macrophages. Science 330, 841–845 (2010).
4. Réu, P. et al. The lifespan and turnover of microglia in the human brain. Cell Rep. 20, 779–784 (2017).
5. Reed, M. D. et al. IL-17a promotes sociability in mouse models of neurodevelopmental disorders. Nature 577, 249–253 (2020).
6. Thion, M. S. et al. Microbiome influences prenatal and adult microglia in a sex-specific manner. Cell 172, 500–516 (2018).
7. Wendeln, A. C. et al. Innate immune memory in the brain shapes neurological disease hallmarks. Nature 556, 332–338 (2018).
8. Liu, Y. J. et al. Microglia elimination increases neural circuit connectivity and activity in adult mouse cortex. J. Neurosci. 41, 1274–1287 (2021).
9. Cruz-Carrillo, G. & Camacho-Morales, A. Metabolic flexibility assists reprograming of central and peripheral innate immunity during neurodevelopment. Mol. Neurobiol. 58, 703–718 (2020).
10. Shin Yim, Y. et al. Reversing behavioural abnormalities in mice exposed to maternal inflammation. Nature 549, 482–487 (2017).
11. Smolders, S., Notter, T., Smolders, S. M. T., Rigo, J. M. & Brône, B. Controversies and prospects about microglia in maternal immune activation models for neurodevelopmental disorders. Brain Behav. Immun. 73, 51–65 (2018).
12. Keren-Shaul, H. et al. A unique microglia type associated with restricting development of Alzheimer's disease. Cell 169, 1276–1290 (2017).
13. Olah, M. et al. Single cell RNA sequencing of human microglia uncovers a subset associated with Alzheimer's disease. Nat. Commun. 11, 6129 (2020).
14. Sousa, C. et al. Single-cell transcriptomics reveals distinct inflammation-induced microglia signatures. EMBO Rep. 19, e46171 (2018).
15. Li, Q. et al. Developmental heterogeneity of microglia and brain myeloid cells revealed by deep single-cell RNA sequencing. Neuron 101, 207–223 (2019).
16. Masuda, T. et al. Spatial and temporal heterogeneity of mouse and human microglia at single-cell resolution. Nature 566, 388–392 (2019).
17. Tsafaras, G. P., Ntontsi, P. & Xanthou, G. Advantages and limitations of the neonatal immune system. Front. Pediatr. 8, 5 (2020).
18. Schwarz, J. M., Sholar, P. W. & Bilbo, S. D. Sex differences in microglial colonization of the developing rat brain. J. Neurochem. 120, 948–963 (2012).
19. Negishi, H., Taniguchi, T. & Yanai, H. The interferon (IFN) class of cytokines and the IFN regulatory factor (IRF) transcription factor family. Cold Spring Harb. Perspect. Biol. 10, a028423 (2018).
20. Buniello, A. et al. The NHGRI-EBI GWAS Catalog of published genome-wide association studies, targeted arrays and summary statistics 2019. Nucleic Acids Res. 47, D1005–D1012 (2019).
21. Landek-Salgado, M. A., Faust, T. E. & Sawa, A. Molecular substrates of schizophrenia: homeostatic signaling to connectivity. Mol. Psychiatry 21, 10–28 (2016).
22. Owen, M. J., Sawa, A. & Mortensen, P. B. Schizophrenia. Lancet 388, 86–97 (2016).
23. Sherwood, R. I. et al. Discovery of directional and nondirectional pioneer transcription factors by modeling DNase profile magnitude and shape. Nat. Biotechnol. 32, 171–178 (2014).
24. Qu, K. et al. Individuality and variation of personal regulomes in primary human T cells. Cell Syst. 1, 51–61 (2015).
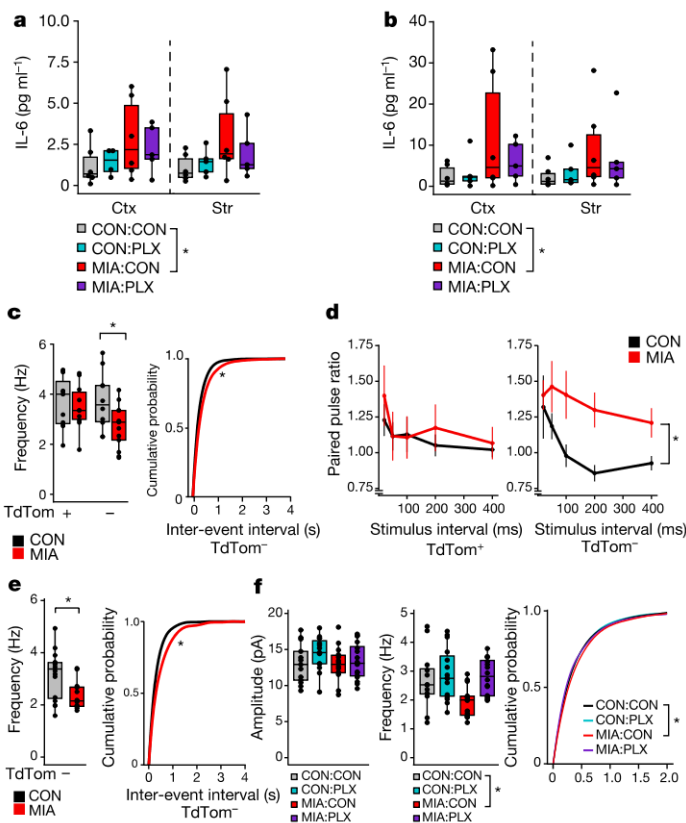
Fig. 5 | Rescue of astrocyte and neuronal phenotypes in MIA using prenatal microglia replacement. a,b, Protein expression of cytokine IL-6 in astrocytes (**a**) and non-astrocyte/non-microglial cells (negative) (**b**) from CON:CON (grey), CON:PLX (cyan), MIA:CON (red) and MIA:PLX (purple) offspring. n values represent individual samples of pooled mice. Statistical analysis was performed using two-way ANOVA with Dunnett's post hoc test. **c**, sEPSCs from DRD1A–TdTomato+ (D1R, TdTom+) and DRD1A–TdTomato− (D2R, TdTom−) MSNs. n values represent individual cells. Statistical analysis was performed using two-sided t-tests, with cumulative distribution analysed using Kolmogorov–Smirnov tests. TdTom+: $n = 11$ (CON:D1R) and $n = 10$ (MIA:D1R); TdTom−: $n = 10$ (CON:D2R) and $n = 13$ (MIA:D2R). $t_{19} = 0.4$, $P = 0.7$ (D1R), $t_{16} = 2$, $P = 0.03$ (D2R); Kolmogorov–Smirnov test, $D = 0.4$, $P = 0.004$ (D2R). **d**, Paired pulse ratio (PPR) with a 20–400 ms interstimulus interval from TdTom+ (D1R) and TdTom− (D2R) MSNs. n values represent individual cells. Data are mean ± s.e.m. Statistical analysis was performed using repeated-measures two-way ANOVA. TdTom+: $n = 14$ (CON:D1R) and $n = 11$ (MIA:D1R); TdTom−: $n = 13$ (CON:D2R) and $n = 11$ (MIA:D2R). Group: $F_{1,110} = 0.99$, $P = 0.32$ (D1R); $F_{1,108} = 14.5$, $P = 0.0002$ (D2R). **e**, mEPSC frequency from D2R (TdTom−) MSNs. n values represent individual cells. Statistical analysis was performed using two-sided t-tests, with cumulative distribution analysed using Kolmogorov–Smirnov tests. $n = 16$ (CON:D2R) and $n = 12$ (MIA:D2R). For D2R, $t_{25} = 3$, $P = 0.01$; Kolmogorov–Smirnov test, $D = 0.4$, $P = 0.008$. **f**, mEPSC amplitude (left) and frequency (centre) of D2R MSNs (TdTom−) from CON:CON (grey), CON:PLX (cyan), MIA:CON (red) and MIA:PLX (purple) with a cumulative distribution plot for mEPSC frequency (right). n values represent individual cells. Statistical analysis was performed using a linear mixed-effect model and Kolmogorov–Smirnov test for the cumulative distribution. Amplitude and frequency: $n = 13$ (CON:CON), $n = 15$ (CON:PLX), $n = 14$ (MIA:CON) and $n = 16$ (MIA:PLX). *$P < 0.05$. The box plots in **a–c**, **e** and **f** show the median (centre line), the IQR (box limits) and 1.5 × IQR (whiskers). Details of the statistical analyses are shown in Supplementary Table 1.

account for an enigma in clinical studies in which patients with schizophrenia show increased cytokine levels in the cerebrospinal fluid, but brain imaging data suggest that there is no major increase, or even that there is a decrease, in cellular immune activation[37–39]. We determined a hypoactivation of microglia while showing an increased inflammatory

Article

25. Klemm, S. L., Shipony, Z. & Greenleaf, W. J. Chromatin accessibility and the regulatory epigenome. *Nat. Rev. Genet.* **20**, 207–220 (2019).
26. Bentsen, M. et al. ATAC-seq footprinting unravels kinetics of transcription factor binding during zygotic genome activation. *Nat. Commun.* **11**, 4267 (2020).
27. Karabacak Calviello, A., Hirsekorn, A., Wurmus, R., Yusuf, D. & Ohler, U. Reproducible inference of transcription factor footprints in ATAC-seq and DNase-seq datasets using protocol-specific bias modeling. *Genome Biol.* **20**, 42 (2019).
28. Kang, C. et al. The DNA damage response induces inflammation and senescence by inhibiting autophagy of GATA4. *Science* **349**, aaa5612 (2015).
29. Mogensen, T. H. IRF and STAT transcription factors—from basic biology to roles in infection, protective immunity, and primary immunodeficiencies. *Front. Immunol.* **9**, 3047 (2018).
30. Villarino, A. V., Kanno, Y. & O'Shea, J. J. Mechanisms and consequences of Jak-STAT signaling in the immune system. *Nat. Immunol.* **18**, 374–384 (2017).
31. Ramirez, R. N. et al. Dynamic gene regulatory networks of human myeloid differentiation. *Cell Syst.* **4**, 416–429 (2017).
32. Camp, J. G. et al. Microbiota modulate transcription in the intestinal epithelium without remodeling the accessible chromatin landscape. *Genome Res.* **24**, 1504–1516 (2014).
33. Li, K. et al. Landscape and dynamics of the transcriptional regulatory network during natural killer cell differentiation. *Genomics Proteomics Bioinform.* **18**, 501–515 (2020).
34. Meers, M. P., Bryson, T. D., Henikoff, J. G. & Henikoff, S. Improved CUT&RUN chromatin profiling tools. *eLife* **8**, e46314 (2019).
35. Skene, P. J. & Henikoff, S. An efficient targeted nuclease strategy for high-resolution mapping of DNA binding sites. *eLife* **6**, e21856 (2017).
36. Luchicchi, A. et al. Maternal immune activation disrupts dopamine system in the offspring. *Int. J. Neuropsychopharmacol.* **19**, pyw007 (2016).
37. Hayes, L. N. et al. Inflammatory molecular signature associated with infectious agents in psychosis. *Schizophr. Bull.* **40**, 963–972 (2014).
38. Coughlin, J. M. et al. In vivo markers of inflammatory response in recent-onset schizophrenia: a combined study using [(11)C]DPA-713 PET and analysis of CSF and plasma. *Transl. Psychiatry* **6**, e777 (2016).
39. Conen, S. et al. Neuroinflammation as measured by positron emission tomography in patients with recent onset and established schizophrenia: implications for immune pathogenesis. *Mol. Psychiatry* **26**, 5398–5406 (2021).
40. Taneja, V. Sex hormones determine immune response. *Front. Immunol.* **9**, 1931 (2018).
41. Hanamsagar, R. et al. Generation of a microglial developmental index in mice and in humans reveals a sex difference in maturation and immune reactivity. *Glia* **65**, 1504–1520 (2017).

Methods

Animal husbandry

All of the animal procedures were approved by the IACUC at Johns Hopkins University. Animals were maintained in individually ventilated cages under a 14 h–10 h light–dark cycle and allowed food and water ad libitum in a temperature- and humidity-controlled facility (22 ± 3 °C, 45 ± 5%). The mice were maintained on a standard diet of 18% protein (sterilized 2018SW, Envigo). C57BL/6J mice were purchased from Jackson labs (00664), dopamine receptor D1alpha-TdTomato (DRD1A–TdTomato) mice were shared by G. Dölen backcrossed to the C57BL/6J mouse line. Male mice were used for breeders and mated with wild-type females to generate CON and MIA pups. Male mice were used for the majority of experiments (see Extended Data Fig. 10 for data from male and female mice).

Generation of MIA and microglia replacement

To generate MIA pups, virgin female mice (C57BL/6J, aged 8–12 weeks) were plug checked each morning after mating and the appearance of a vaginal plug was demarcated as embryonic day 0.5. The timed-pregnant females were delivered PIC (Sigma-Aldrich, P9582) by intraperitoneal injection (i.p.) between 08:00 and 11:00 on E9.5. PIC or SAL was delivered 10–20 mg kg^{-1} at a volume five times the animal weight (5 ml kg^{-1}). We used E9.5 as our MIA timepoint because this is when the microglia infiltrate the neuroepithelium[3]. To ensure efficacy of the maternal immune event, we monitored IL-6 protein expression in the maternal serum 3–4 h after injection. Maternal immune responses below 1,000 pg ml^{-1} were excluded (Extended Data Fig. 10e). Each new batch of PIC was quality controlled to ensure that it elicited a comparable immune response, and we found that a serum response of greater than 20 ng ml^{-1} led to a severe loss of pup viability (Extended Data Fig. 10e). For rescue experiments, pregnant dams were placed on PLX5622 (Plexxikon, colony stimulator factor 1 receptor antagonist) or control chow for 3 days between E9.5 to E12.5. On E12.5, mice were returned to house chow.

LPS injection

LPS (Sigma-Aldrich, L4391) was reconstituted in SAL to a concentration of 600,000 endotoxin units per ml. Peripheral LPS was injected by IP at a dose of 4,500 endotoxin units per g body weight. Serum IL-6 was measured at 18 h after injection to ensure responsiveness.

Blood draw

Peripheral immune response was monitored to establish a threshold for responsiveness. To collect blood, mice were immobilized and the mandibular/facial vein was pricked with a 4 mm lancet or the tail end was snipped to collect blood drops into a 1.5 ml tube. The blood was allowed to clot for at least 15 min and was then centrifuged at 9,000 rpm for 5 min twice and the supernatant was collected and frozen until assayed.

Enzyme-linked immunosorbent assay

Cytokines in the serum and cell culture supernatant were measured using the eBioscience Ready-Set-Go ELISA kits according to the manufacturer's instructions. In brief, 96-well plates were coated with capture antibodies for either IL-6 or TNFα overnight. The plates were washed in buffer, blocked for 1–2 h with 1× assay diluent, and then diluted standards and samples were incubated in the plate overnight. Finally, the plate was washed, treated with detection and HRP antibodies, and developed using TMB reaction with a nitric acid stop solution. The colorimetric signal was measured on a plate reader at 450 nm subtracted by 570 nm (Bio-Rad). Maternal serum was diluted 1:100, cell culture supernatants were diluted 1:50 and LPS response serum was diluted 1:10.

Cell homogenates were measured using a more sensitive ELISA kit (V-Plex, Mesoscale Discovery). Cells were isolated by sequential MACS

sorting for microglia (CD11b) then the flow-through was stained for ACSA2 to isolate astrocytes, and the final flow-through was collected as the negative fraction. The cells were homogenized using RIPA buffer (150 mM NaCl, 1% NP40, 0.1% SDS, 0.5% sodium deoxycholate, 50 mM Tris-HCl, 1× protease inhibitor) with sonication, insoluble protein was pelleted and soluble protein was quantified using the Micro BCA Protein Assay (Thermo Fisher Scientific). IL-6, TNFα and IL-1β were measured according to the manufacturer's instructions. In brief, the plate was washed three times before adding the diluted samples (1 mg ml^{-1}) and standards for 2 h. The multiplex plate was washed three times and the detection antibody was incubated for 2 h. Finally, the plate was washed three times, 2× read buffer was applied, the plate was read on an MSD plate reader and analysed using the MSD Workbench software.

Immunohistochemistry

Embryos or tissue sections were collected and fixed overnight in 4% paraformaldehyde then cryopreserved in 15% and 30% sucrose. Embryonic tissue was frozen in OCT in a bath of isopentane cooled in liquid nitrogen and then cryosectioned on a Leica cryostat at 12–15 μm sections. Adult tissue sections were sectioned on a Leica vibratome at 50 μm and stored at 4 °C. For immunostaining, the sections were rinsed in PBT (1X PBS, 0.2% Triton-X100), blocked in 10% normal donkey serum and then stained with antibodies overnight (rabbit anti-IBA1, 1:500, Wako (019-19741) and rat anti-mouse CD68, 1:100, Bio-Rad (MCA1957)). The next day, the sections were rinsed in PBT three times, stained with secondary antibodies (donkey anti-rabbit Alexa 488, 1:500, Thermo Fisher Scientific (A32790) and donkey anti-mouse Alexa 555, 1:500, Thermo Fisher Scientific (A31570)) then counterstained with DAPI, and mounted in aqueous mounting medium (fluoromount-g). Images were captured on the Keyence microscope at ×10 magnification. High-resolution images were collected on the Zeiss AxioObserver D1 at ×20 and images were tiled and enhanced with Adobe Photoshop. Confocal images were captured on a Zeiss LSM 880 Confocal. z-Stacks were collected at 0.5 μm z-intervals for the entire stack at ×63 magnification. Low-magnification images were taken at ×10 with a 2 μm z-stack interval.

Microglia morphology and density analysis

All microglia density and morphology analyses were performed blinded to the condition. Using Imaris (x64 v.9.5.1), we quantified the microglia density in the striatum. Using the spots tool, microglia were automatically identified (settings: 10 μm diameter with background subtraction). All cells were verified by eye before final quantification based on image area and volume. Three to four images per region (dorsal or ventral striatum) per animal were analysed. Data were analysed on the basis of per animal density averages per region and statistical analysis was performed using a three-way ANOVA.

Microglia morphology was analysed by Sholl analysis in Imaris. Specifically, individual microglia were surface-rendered based on the IBA1 channel and individual cell masks were cropped for Sholl analysis. Next, using the filament tool, individual microglia were traced using the default settings (no spine detection and cell body sphere region ~10–11 μm) and manually modified if necessary. Finally, microglia and lysosomal volume was calculated using the surface tool. Specifically, the microglia (IBA1 signal) from the individually cropped cells were used to calculate the CD68 surface volume within the IBA1 volume. The CD68 signal was rendered using settings: local contrast, diameter = 1 μm, greater than 5 voxels, filtered to shortest distance to surfaces. The volume of each individual microglia, the volume of total lysosomes in microglia and the percentage of microglia volume containing lysosomes were calculated.

Microglia in vitro culture

The brains from an entire E18 litter (both male and female) were pooled. After meningeal removal, the cortex was collected, hippocampi removed, and the subcortical striatum or cortex was collected into

separate tubes. The tissue was mechanically homogenized using 18, 22 and 25 gauge needles successively. After filtering, the cell suspension was plated into T75 culture flasks (5 million cells per flask) coated with poly-D-lysine (100 μg ml^{-1}, final). The medium (DMEM/F12, 10% heat-inactivated FBS, 1% penicillin–streptomycin) was changed every 3–5 days and M-CSF was supplemented (Peprotech 315-02, 5 ng ml^{-1}) for 2 weeks. Previous studies isolated microglia by shaking the flasks at 200–250 rpm for 4–5 h and then collecting and plating the floating microglia cells in the supernatant[43,44]. We found that we could get comparable experimental results, but more cell yield when we collected all the cells in the flask with trypsin, and isolated microglia through magnetic sorting with CD11b magnetic beads. We found that both methods gave similar results and, therefore, both are combined in the data. To perform the magnetic sorting, the flasks were briefly treated with trypsin to release the cells, inactivated with complete medium and washed with magnetic sorting buffer (PBS, 2 mM EDTA, 0.5% BSA). The cells were treated with CD11b magnetic beads for 30 min, washed with magnetic sorting buffer and isolated on a magnetic column after washing. The cells were plated in a 96-well plate at 40,000 cells per well overnight. The cells were treated with LPS (100 ng ml^{-1}) and IFNγ (10 ng ml^{-1}) for 12 h and the cell culture supernatant was collected, centrifuged at maximum speed to remove any debris and frozen until assayed.

The adult animals (aged 8–10 weeks) were deeply anaesthetized with ether, perfused with PBS and the brains were isolated. The meninges were removed and then the frontal cortex and striatum were collected into 2 ml tubes. We pooled two mice of the same sex for each culture and used both males and females. The brain pieces were diced with scissors and then homogenized with papain according to the adult neural dissociation kit (Miltenyi). In brief, the tissue was treated with papain and DNase at 37 °C for 30 min with rotation. The homogenates were pipetted gently and filtered with a 70 μm strainer. The cell pellet was resuspended in debris-removal solution (300 μl debris removal, 700 μl PBS), overlaid with 300 μl of PBS, centrifuged at 3,000g for 10 min and debris was aspirated, and the sample washed with PBS and centrifuged at 1,000g for 10 min. The cell suspension was then plated in T25 flasks coated with poly-L-lysine (15 μg ml^{-1}). The medium was changed every 3–4 days and supplemented with M-CSF (10 ng ml^{-1}). After 2 weeks, the microglia were isolated by magnetic sorting and stimulated as described above. For in vitro experiments, cytokine measurements were normalized to the cell density as measured by a 1 h Alamar Blue assay according to the manufacturer's instruction (Invitrogen).

Microglia isolation

Male mice (aged 8–10 weeks) were deeply anaesthetized with ether, perfused with PBS and the brains were extracted. The meninges were removed and then the frontal cortex and striatum were collected into 2 ml tubes with HBSS on ice. The frontal cortex was collected from a coronal slice anterior to 1.7 mm bregma and dorsal of the corpus callosum, and the anterior striatum was excised from this slice by collecting the tissue surrounding the nucleus accumbens. The next coronal slice was cut at −0.5 bregma and the dorsal and ventral striatum was excised from this slice, excluding the olfactory tubercle, and all of the striatum pieces were pooled together. Neonatal (P4) mice were not perfused, but blood was drained by decapitation. The brain pieces were diced with scissors and then homogenized with enzymes according to the adult neural dissociation kit (Miltenyi) as described above. The cells were resuspended in 0.5% BSA in HBSS. For magnetic sorting, anti-CD11b magnetic beads were added for 30 min at 4 °C. The cells were washed with buffer and isolated on the magnetic column before final collection into lysis buffer. For sequential collection, the flow-through negative cells were collected and treated with ACSA2 magnetic beads for 30 min before washing and again collecting on a magnetic column. The collected astrocytes and uncaptured flow-through cells were both collected and lysed in lysis buffer. For fluorescence-activated cell sorting (FACS) sorting, the cells were incubated with Fc block (1:50,

eBioscience, 16-0161-81) for 5 min then incubated with antibodies for CD45-APC (1:100, BD Biosciences 561018) and CD11b-BV421 (1:100, BD Biosciences 562605) for 30 min, the cells were washed twice with buffer times before filtering and collecting on a MoFlo Legacy system. Cells were gated on the basis of size, singlet and propidium iodide negative (live cells), before sorting on CD45–APC low, CD11b–BV421 positive (Extended Data Fig. 10f).

Quantification of embryonic myeloid cells by FACS

Pregnant dams were euthanized by cervical dislocation and the pups quickly removed. The brains were extracted on ice and the meninges were removed. Whole brains from individual animals were placed in a tube with papain and DNase (Miltenyi adult neural dissociation kit) and digested for 20–30 min at 37 °C. The solution was pipetted through a 70 μm strainer and centrifuged at 2,500 rpm for 2 min to collect the cells. Debris was removed using a debris-removal solution (Miltenyi, as above). The cells were incubated with Fc block (eBioscience, 16-0161-81) for 5 min then incubated with antibodies (CD45–APC BD Biosciences, 561018; and CD11b–BV421 BD Biosciences, 562605) for 30 min at 4 °C in FACS buffer (0.5% BSA, 2 mM EDTA, 25 mM HEPES, in 1× HBSS), washed well and strained though a 40 μm strainer. Cells were gated on size (singlet) and propidium iodide negative (live cells), before quantifying on CD45–APC$^+$, CD11b–BV421$^+$ cells using the MoFlow XDP sorter (Extended Data Fig. 7d).

RNA isolation for qPCR with reverse transcription and bulk RNA-seq

RNA was collected from freshly isolated, flash-frozen tissue or sorted cells according to the kit instruction (Qiagen, Micro-RNAeasy, PicoPure RNA isolation Kits). Single-stranded cDNA synthesis was prepared from purified RNA using oligo-dT and a random hexamer primer mix with superscript III or IV according to the manufacturer's instructions (Thermo Fisher Scientific). qPCR was performed using Taqman or SYBR green master mix and 1 μM mix of forward and reverse primers. The samples were run on a 7900 HT real-time PCR machine with the following cycles: 95 °C for 10 min; 40–50 cycles of 95 °C for 15 s, 60 °C for 30 s and 72 °C for 30 s; and 72 °C for 10 min. The melting curve was evaluated for single peak and a standard curve was performed to ensure linear amplification of each primer set. The following primer sets were used: *Iba1* (TaqMan Mm01132452_g1), *Tnf* (forward, CCCTCACACTCAGAT-CATCTTCT; reverse, GCTACGACGTGGGCTACAG), *Gapdh* (forward, TGCAGTGGCAAAGTGGAGATT; reverse. TTGAATTTGCCGTGAGTGGA); *Gapdh* (TaqMan Mm99999915_g1). Relative expression was calculated by subtracting the average endogenous control (*Gapdh*) C_t values from each target gene C_t value to generate a ΔC_t value. The fold change was then calculated by setting the CON cortex sample to one and calculating the $2^{-\Delta C_t}$ for each sample. Data were log-normalized for analysis.

Electrophysiology

Acute parasagittal brain slices (250 μm) containing the nucleus accumbens (NAc) core were prepared from male heterozygous DRD1A–tdTomato transgenic mice (aged 9–12 weeks). In brief, the mice were anaesthetized with isoflurane and the brains were quickly dissected and placed in ice-cold sucrose solution containing 76 mM NaCl, 75 mM sucrose, 25 mM D-(+)-glucose, 25 mM NaHCO$_3$, 2.5 mM KCl, 1.25 mM NaH$_2$PO$_4$, 0.5 mM CaCl$_2$, 7 mM MgSO$_4$ finally equilibrated to pH 7.3–7.4 with 310 mOsm. Slices were prepared with a vibratome (VT1200S, Leica) in oxygenated (95% O$_2$, 5% CO$_2$) ice-cold sucrose solution and recovered in warm (32–34 °C) oxygenated sucrose solution for 30 min. The slices were transferred to warm (32–34 °C) oxygenated artificial CSF (aCSF) containing 125 mM NaCl, 20 mM D-(+)-glucose, 26 mM NaHCO$_3$, 2.5 mM KCl, 1.25 mM NaH$_2$PO$_4$, 1 mM MgSO$_4$, 2 mM CaCl$_2$ supplemented with 0.4 mM ascorbic acid, 2 mM pyruvic acid and 4 mM L-lactic acid, finally equilibrated to pH 7.3–7.4 with 315 mOsm, and then cooled to room temperature until recording. Slices were transferred to a submersion chamber and continuously superfused

(3–4 ml min^{-1}) with warm oxygenated aCSF (32 °C) containing 100 μM of picrotoxin while recording. MSNs located in anterior-dorsal part of NAc were visually identified with an upright microscope (Olympus BX51WI equipped with ×40/0.8 NA objective) using either transmitted light with IR-DIC optics or epifluorescence signal through digital CMOS camera (ORCA-Flash 4.0 LT, Hamamatsu). For the whole-cell patch, microglass recording electrodes (3–5 MΩ) were filled with internal solution containing 120 mM CsMeSO$_4$, 15 mM CsCl, 8 mM NaCl, 10 mM HEPES, 0.2 mM EGTA, 10 mM TEA-Cl, 4 mM MgATP, 0.3 mM NaGTP, 0.1 mM spermine and 5 mM QX-314, pH 7.3 with 290 mOsm and recordings were obtained with the Multiclamp 700B amplifier (Molecular Devices) controlled by pClampex 10.3 (Molecular Devices), filtered 2 kHz and digitized at 10 kHz with Digidata 1440A (Molecular Devices). Excitatory afferent fibres located between the NAc core and cortex dorsal to the anterior commissure were stimulated with a bipolar concentric electrode (FHC) with an intensity that can induce 100–300 pA of EPSCs at −70 mV. Access resistance was monitored throughout the experiments by applying a mild hyperpolarizing pulse in each sweep and only the results from the cells changing less than 20% were used for further analysis. *I*/*V* relationships were acquired with afferent fibre stimulation while changing the holding potential. Rectification indexes for AMPA receptors were calculated by the ratio of the peak amplitudes at +40 mV and −70 mV, respectfully. AMPAR/NMDAR ratios were obtained by dividing the peak amplitude of EPSCs at −80 mV (AMPAR EPSCs) by the magnitude of EPSCs at +40 mV at 50 ms after stimulation (NMDAR EPSCs). Paired-pulse ratios were acquired by dividing EPSC2 by EPSC1 obtained from a paired afferent stimulation with the same stimulating intensity by the designated interstimulus interval. Spontaneous EPSCs were recorded at −70 mV for 1 min while monitoring access resistance in every 15 s. Electrophysiology data were displayed off-line with Clampfit software (Molecular Devices). Analysis of spontaneous EPSCs was performed using MiniAnalysis software (Synaptosoft) by automatically detecting negative-going inward EPSCs at a threshold of 5 pA (3 × (RMS of noise)$^{1/2}$) and each event was manually inspected. Instantaneous amplitudes and frequencies were acquired to obtain the mean value and cumulative graph.

Spine counting

Spine counting was performed on golgi-stained tissue (FD Rapid GolgiStain Kit). In brief, male mice were decapitated and the brains were rapidly extracted. The whole brain was rinsed in water and placed in impregnation solution for 9 days, then transferred to solution C. After 3 days in solution C, the brains were frozen in isopentane, 150 μm sections were collected on a cryostat (Leica) and mounted onto gelatin-coated microscope slides. The sections were then rinsed, stained for golgi and dehydrated before mounting in permount. The spines were quantified using the Zeiss AxioImager microscope and the Neurolucida Software (Microbrightfield). The dorsal and ventral striatum was outlined at low magnification, then cells were selected at ×25 and spines were quantified at ×100. We quantified spines that were at 20–200 μm away from the cell body on second- to fifth-order dendrites. We counted 29–41 cells per group/region and averaged the spine density per animal. *n* represents the number of animals.

CUT&RUN

After perfusion, the whole brain was extracted and the cerebellum was removed. The brain was homogenized using a Dounce homogenizer (without enzymes) and microglia were prepared for FACS sorting as described above. Transcription factor DNA occupancy was confirmed using CUT&RUN[34,35] using a commercial kit from Cell Signaling Technology (86652) according to the kit instructions. The cell suspension was stained with Zombie-NIR fixable viability stain. The cells were then fixed according to the kit instructions immediately after FACS antibody staining, and stopped with glycine. A total of 80,000–100,000 microglia were FACS sorted from the whole brain (CD45$^+$, CD11b$^+$, P2RY12$^+$

(BioLegend 848003), Zombie NIR$^-$ (BioLegend 423105)). The cells were captured with concanavalin A beads and incubated with antibodies against IRF1 or STAT2 (Cell Signaling, 8478T, 72604S). The DNA around the transcription factor was cleaved with pAG-MNase and activated in the presence of calcium. The DNA was purified on a column (Cell Signaling, 14209) and targets were quantified using qPCR (Cell Signaling, 88989) for the targets *Fas*, *Il6* and *Il23a*. The targets were quantified as the percentage of the total input DNA from the same number of cells and normalized to a spike-in control DNA. The qPCR sequences for the DNA targets were: *Fas* forward, CCAATTCAATACAGAGTTCAG; *Fas* reverse, CAGGGCTTGATTGCATAAATG; *Il6* forward, CCCAGCTTTAACACAATTTCACTG; *Il6* reverse, AGAAAACCGTGCAATAGACAGGA; and *Il23a* forward, CCCGACCTAGGCCTCTAG; *Il23a* reverse, GCCCGCCCTTCACACTA.

Bulk RNA-seq

Bulk cell RNA-seq libraries were prepared using a modified Smart-Seq2 protocol[45]. Purified RNA (5 ng) was mixed with 2.5 mM dNTP mix, 2.5 μM oligo-dT$_{30}$VN and 1 U μl^{-1} RNasin, and incubated at 72 °C for 3 min. Then, 5.7 μl of the single-cell reverse transcription mix (1× superscript II buffer, 1 M betaine, 5 mM DTT, 100 U superscript II, 10 U RNasin, 1 μM TSO oligo, 6 mM MgCl$_2$) was added to each sample for reverse transcription. The cDNA was amplified using the KAPA HF Ready mix with 9 PCR cycles. The cDNA was cleaned up with AMPure XP beads (Beckman Coulter) at a ratio of 0.7:1, washed with 80% ethanol and resuspended in 17.5 μl water. The libraries were tagmented for sequencing using the Illumina Nextera XT DNA sample preparation kit. cDNA (200–250 pg) was added to 2.5 μl tagment DNA buffer (Illumina) and 1.25 μl of amplicon tagment mix (Illumina) and incubated at 55 °C for 5 min to tagment the cDNA. The reaction was neutralized with 1.25 μl of neutralize tagment buffer and incubated at room temperature for 5 min. The tagmented DNA was then indexed and amplified with 3.75 μl of PCR master mix (Illumina) and 1.25 μl each of the i5 and i7 indexing primers (Illumina, diluted 1:5). The samples were indexed with the following PCR cycles: 1 cycle of 72 °C for 3 min and 95 °C for 30 s; 12 cycles of 95 °C for 10 s, 55 °C for 30 s and 72 °C for 30 s; and 1 cycle of 72 °C for 5 min. The final libraries were purified using AMPure XP beads (Beckman Coulter) at a 0.6:1 ratio, washed with 80% ethanol and resuspended in 12 μl water. The indexed libraries were pooled together at an equal mass ratio for final sequencing on the NovaSeq 6000 system.

Single-cell RNA-seq

Male mice (aged 8–10 weeks) were deeply anaesthetized, perfused with HBSS, brains were extracted, and the frontal cortex and striatum were collected into glass tissue homogenizers on ice with homogenization buffer (15 mM HEPES, 5% trehalose, 500 U ml^{-1} DNase I, 80 U ml^{-1} RNasin, in 1× HBSS)[46]. The brain pieces were homogenized 6–7 times, filtered through a 70 μm strainer and centrifuged at 2,500 rpm for 2 min to collect the cells. Debris and myelin was removed using a debris-removal solution (Miltenyi, see above). The cells were incubated with Fc block (eBioscience, 16-0161-81) for 5 min then incubated with antibodies (CD45-APC BD Biosciences, 559864; and CD11b-BV421 BD Biosciences, 562605) for 30 min at 4 °C in incubation buffer (0.5% BSA, 2 mM EDTA, 25 mM HEPES, 5% trehalose, 80 U ml^{-1} RNasin in 1× HBSS), washed well with FACS buffer (0.5% BSA, 2 mM EDTA, 25 mM HEPES, in 1× HBSS) and strained though a 40 μm strainer. Cells were gated on the basis of size, singlet and propidium iodide negative (live cells), before sorting on CD45-APC low, CD11b-BV421 positive using a MoFlo Legacy sorter. Single cells were captured on the 10x Genomics Chromium Platform at a capture target of 6,000–10,000 cells. The libraries were pooled and sequenced on the NovaSeq 6000 system.

ATAC-seq

Single cells were prepared and FACS-sorted as described above. A total of 12,500–25,000 cells were collected for each ATAC sample.

Article

The ATAC libraries were prepared as described previously[47]. In brief, cells were pelleted by centrifuging at 500g for 15 min at 4 °C, and the supernatant was carefully removed. Cell lysis buffer (50 µl) was added (10 mM Tris-HCl, 10 mM NaCl, 3 mM MgCl$_2$, 0.1% NP-40, 0.1% Tween-20, 0.01% digitonin), pipetted to mix 3–5 times, incubated on ice for 3 min and washed (10 mM Tris-HCl, 10 mM NaCl, 3 mM MgCl$_2$, 0.1% Tween-20). The nuclei were centrifuged to pellet at 500g for 30 min at 4 °C and the supernatant was carefully removed. The Tn5 buffer (1× TD buffer, 1× PBS, 0.1% Tween-20, 0.01% digitonin, 1 µl Tn5) was then added and incubated at 37 °C for 1 h under shaking at 1,000 rpm. The DNA was collected using the Qiagen Minelute clean-up kit. The DNA was eluted with 11 µl EB buffer. For library preparation, 10 µl of prepared DNA was mixed with 1.25 µM indexing primers and 1× NEBNext High-Fidelity PCR Master Mix and amplified (72 °C for 5 min; 98 °C for 30 s; then 5 cycles of 98 °C for 10 s, 63 °C for 30 s and 72 °C for 1 min). Then, 5 µl was used for qPCR to test amplification and calculate additional cycles. Then, 6–8 more cycles were run before clean-up with Ampure XP beads. The libraries were quality control checked using a Bioanalyzer and then pooled at equal mass for sequencing on the NovaSeq 6000 system.

RNA-seq analysis

The FASTQ files were first quality checked using FASTQC. The libraries were aligned, assembled and quantified using RSEM with the STAR aligner (rsem-calculate-expression) using the GRCm38 primary assembly and gencode vM25 primary assembly annotation. Samples were excluded if they were determined to be an outlier due to isolated clustering using two methods (principal component analysis (PCA) and hclust). Further analysis was performed in R using pipelines for DESeq2[48,49] and additional modelling with edgeR[50,51]. Gene set enrichment analyses (Broad, GSEA 4.1.0 build 27)[52] were used for pathway analysis with graphical rendering using cytoscape (v.3.8.2)[53]. Gene enrichment for disease association was performed with data from the NHGRI GWAS catalog (v.1.0.2; https://www.ebi.ac.uk/gwas/) and included genes with a −log$_{10}$-transformed $P > 8$ and an odds ratio of >1 for associations with autism, attention deficit hyperactivity disorder, bipolar disorder, depression and schizophrenia were counted with the DEGs and non-DEGs using a χ^2 test between the MIA microglia DEGs and the non-DEGs with Bonferroni and Benjamini–Hochberg correction for multiple comparisons.

Single-cell RNA-seq analysis

Single-cell libraries were aligned and quantified using the 10x genomics cloud Cell Ranger Count v.6.0.0. The libraries were analysed using Seurat (v.4)[54]. Doublets were estimated with scDblFinder[55]. Low-quality cells were filtered using RNA count < 600, feature detected < 500, and percent mitochondrial reads > 10%. The cells from each sample were integrated using SCTransform with glmGamPoi and reciprocal PCA using Seurat[56,57], dimension reduction with PCA and UMAP, and neighbourhood and cluster detection with a resolution of 0.2 (ref. [58]). Cluster-enriched genes were identified using Seurat FindMarkers. Differential abundance was analysed using a t-test and one-way ANOVA for the percentage contribution of each sample to each cluster. Samples with low serum IL-6 protein expression were excluded from the differential abundance analysis.

ATAC–seq analysis

Library quality was assessed using FASTQC. Libraries were trimmed using cutaddapt[59] and aligned using bowtie2[60]. PCR duplicates were identified and removed using PICARD MarkDuplicates (Picard Toolkit, 2019, Broad Institute; http://broadinstitute.github.io/picard/). Peaks were called using MACS2 (-f BAMPE --min-length 100 --max-gap 50)[61]. Coverage and transcriptional start site distances were calculated using DeepTools[62], and peak counts were calculated using FeatureCounts[63] from subread. Differentially accessible regions were identified using DiffBind[64] and a permutation test was used for multiple-comparison correction. For pathway analysis, we used Genomic Regions Enrichment of Annotations Tool (GREAT, v.4.0.4) to identify enriched pathways for the open chromatin regions (http://great.stanford.edu/public/html/). For footprint analysis, the BAM files were shifted for Tn5 correction using alignmentSieve from DeepTools (--ATACshift) and PIQ[26] for footprint detection using the *Homo sapiens* Comprehensive Model Collection (HOCOMOCO) (v.11) motif database[65]. Transcription factor occupancy thresholds were as follows: 0.9 purity score, >250 total occupancy sites and >0.5 log$_2$-transformed fold change between MIA and CON. Transcriptional network analysis of ATAC–seq and RNA-seq data was performed using PECA (v.2.0)[66,67]. Specifically, paired ATAC-seq, RNA-seq and ENCODE data were used to generate transcription factor–target regulation scores indicating the strength and significance of the regulation network. The ENCODE data were used as a training set and to determine the direction of the transcription factor–target regulation (repressor versus activator) using a Pearson's correlation. The transcriptional regulation networks were then compared across the control and MIA. The full likelihood and inference algorithms were reported previously[66,67].

Statistics

Statistical analyses were performed using the statistical computing program R. Analyses that required subjective measurement included blinded spine density, microglia morphology and lysosomal content. A list of the exact sample sizes and full statistical results is provided in Supplementary Table 1. Data were tested for normality using Shapiro–Wilks tests. Normally distributed data were analysed using two-tailed t-tests, and non-normally distributed data were analysed using Wilcoxon rank-sum tests. One- and two-way ANOVAs were performed with pairwise two-sided t-tests with pooled error and Benjamini–Hochberg correction for multiple comparisons. Moreover, we used mixed-effect linear regression with emmeans to estimate marginal means and include litter as a random effect variable.

Reporting summary

Further information on research design is available in the Nature Research Reporting Summary linked to this article.

Data availability

The datasets generated and analysed during this study are available from the corresponding author on reasonable request. Genomics data are available at the NCBI Gene Expression Omnibus under SuperSeries accession number GSE201817. Publicly available databases used in this manuscript include HOCOMOCO (v.11)[65] (https://hocomoco11.autosome.org), ENCODE data from PECA (v.2.0; https://github.com/SUwonglab/PECA)[66,67] and NHGRI GWAS catalog (v.1.0.2; https://www.ebi.ac.uk/gwas/). Source data are provided with this paper.

Code availability

Source codes are available at GitHub (https://github.com/lindsaynhayes/Hayes_2022).

42. Goel, N. & Bale, T. L. Examining the intersection of sex and stress in modelling neuropsychiatric disorders. *J. Neuroendocrinol.* **21**, 415–420 (2009).
43. Tamashiro, T. T., Dalgard, C. L. & Byrnes, K. R. Primary microglia isolation from mixed glial cell cultures of neonatal rat brain tissue. *J. Vis. Exp.* **66**, e3814 (2012).
44. Mecha, M. An easy and fast way to obtain a high number of glial cells from rat cerebral tissue: a beginners approach. *Protocol Exchange* https://doi.org/10.1038/protex.2011.218 (2011).
45. Picelli, S. et al. Full-length RNA-seq from single cells using Smart-seq2. *Nat. Protoc.* **9**, 171–181 (2014).
46. Bennett, M. L. et al. New tools for studying microglia in the mouse and human CNS. *Proc. Natl Acad. Sci. USA* **113**, E1738–E1746 (2016).
47. Corces, M. R. et al. An improved ATAC-seq protocol reduces background and enables interrogation of frozen tissues. *Nat. Methods* **14**, 959–962 (2017).

48. Love, M. I., Huber, W. & Anders, S. Moderated estimation of fold change and dispersion for RNA-seq data with DESeq2. *Genome Biol.* **15**, 550 (2014).
49. Soneson, C., Love, M. I. & Robinson, M. D. Differential analyses for RNA-seq: transcript-level estimates improve gene-level inferences. *F1000Res.* **4**, 1521 (2015).
50. Robinson, M. D., McCarthy, D. J. & Smyth, G. K. edgeR: a Bioconductor package for differential expression analysis of digital gene expression data. *Bioinformatics* **26**, 139–140 (2010).
51. McCarthy, D. J., Chen, Y. & Smyth, G. K. Differential expression analysis of multifactor RNA-seq experiments with respect to biological variation. *Nucleic Acids Res.* **40**, 4288–4297 (2012).
52. Subramanian, A. et al. Gene set enrichment analysis: a knowledge-based approach for interpreting genome-wide expression profiles. *Proc. Natl Acad. Sci. USA* **102**, 15545–15550 (2005).
53. Shannon, P. et al. Cytoscape: a software environment for integrated models of biomolecular interaction networks. *Genome Res.* **13**, 2498–2504 (2003).
54. Hao, Y. et al. Integrated analysis of multimodal single-cell data. *Cell* **184**, 3573–3587 (2021).
55. Germain, P., Lun, A., Macnair, W. & Robinson, M. Doublet identification in single-cell sequencing data using scDblFinder. *F1000 Res.* https://doi.org/10.12688/f1000research.73600.1 (2021).
56. Hafemeister, C. & Satija, R. Normalization and variance stabilization of single-cell RNA-seq data using regularized negative binomial regression. *Genome Biol.* **20**, 296 (2019).
57. Ahlmann-Eltze, C. & Huber, W. glmGamPoi: fitting gamma-Poisson generalized linear models on single cell count data. *Bioinformatics* **36**, 5701–5702 (2021).
58. McInnes, L., Healy, J., Saul, N. & Großberger, L. UMAP: uniform manifold approximation and projection. *J. Open Source Softw.* **3**, 861 (2018).
59. Martin, M. Cutadapt removes adapter sequences from high-throughput sequencing reads. *EMBnet J.* **17**, 10–12 (2011).
60. Langmead, B. & Salzberg, S. L. Fast gapped-read alignment with Bowtie 2. *Nat. Methods* **9**, 357–359 (2012).
61. Zhang, Y. et al. Model-based analysis of ChIP-Seq (MACS). *Genome Biol.* **9**, R137 (2008).
62. Ramírez, F. et al. deepTools2: a next generation web server for deep-sequencing data analysis. *Nucleic Acids Res.* **44**, W160–W165 (2016).
63. Liao, Y., Smyth, G. K. & Shi, W. featureCounts: an efficient general purpose program for assigning sequence reads to genomic features. *Bioinformatics* **30**, 923–930 (2014).
64. Ross-Innes, C. S. et al. Differential oestrogen receptor binding is associated with clinical outcome in breast cancer. *Nature* **481**, 389–393 (2012).
65. Kulakovskiy, I. V. et al. HOCOMOCO: towards a complete collection of transcription factor binding models for human and mouse via large-scale ChIP-Seq analysis. *Nucleic Acids Res.* **46**, D252–D259 (2018).
66. Duren, Z., Chen, X., Jiang, R., Wang, Y. & Wong, W. H. Modeling gene regulation from paired expression and chromatin accessibility data. *Proc. Natl Acad. Sci. USA* **114**, E4914–E4923 (2017).
67. Duren, Z., Chen, X., Xin, J., Wang, Y. & Wong, W. H. Time course regulatory analysis based on paired expression and chromatin accessibility data. *Genome Res.* **30**, 622–634 (2020).

Additional information
Supplementary information The online version contains supplementary material available at https://doi.org/10.1038/s41586-022-05274-z.
**Correspondence and requests for materials** should be addressed to Akira Sawa.
Peer review information *Nature* thanks Vijay Kuchroo and the other, anonymous, reviewer(s) for their contribution to the peer review of this work.
Reprints and permissions information is available at http://www.nature.com/reprints.
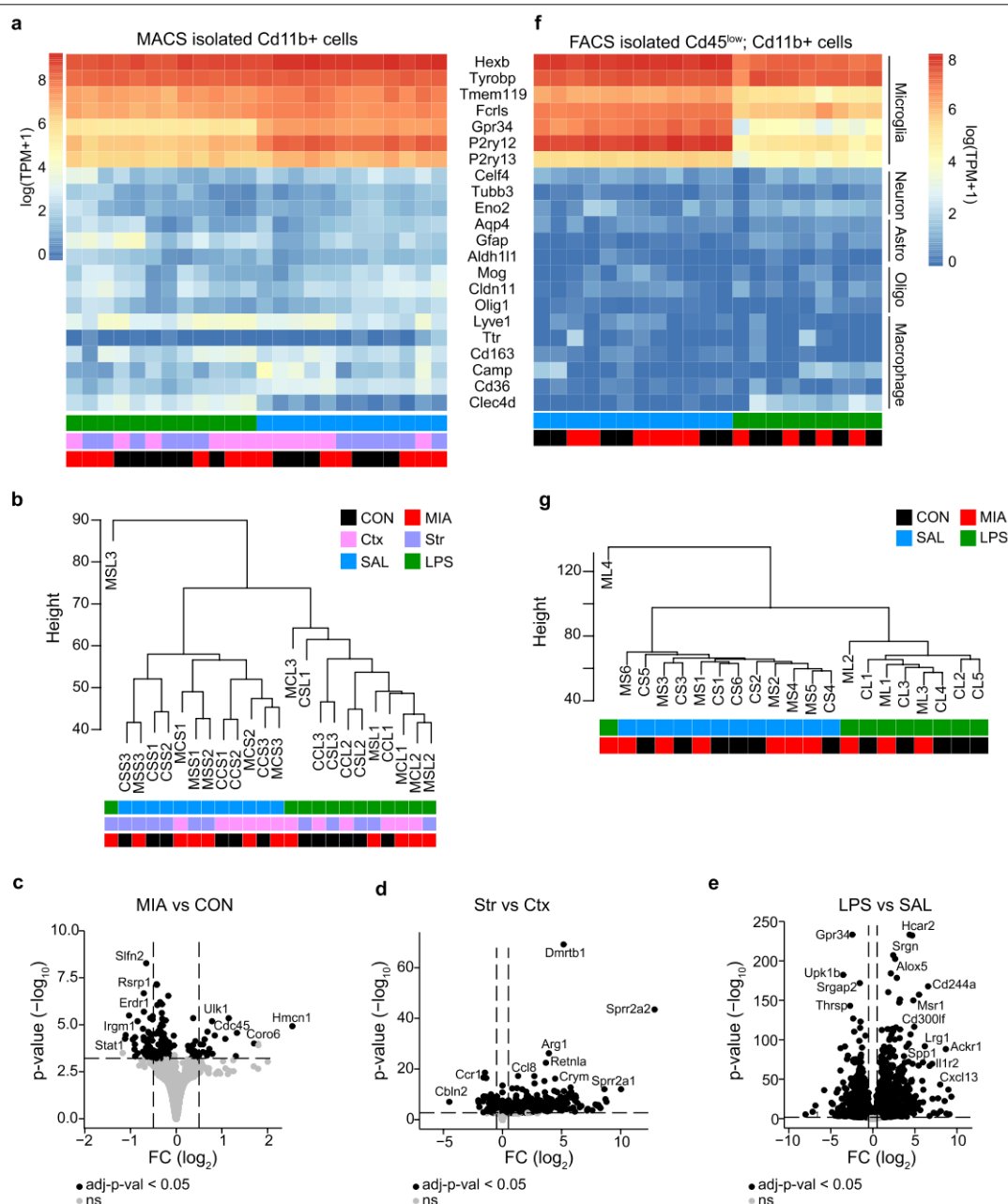
Extended Data Fig. 1 | Quality control data of adult bulk microglia RNA sequencing for Fig 1. a, Heatmap for the gene expression of cell type specific markers for microglia, neurons, astrocytes, oligodendrocytes, and macrophages from MACS-isolated CD11b+ cells. **b**, Clustering of bulk microglia RNA sequencing samples from (a). One outlier identified (MSL3) and removed from subsequent analysis. Sample naming is as follows: first position M (MIA, red) or C (CON, black), second position C [cortex (Ctx), pink] or S [whole striatum (Str), purple], third position S (SAL, blue) or L (LPS, green), fourth position is animal number. **c–e**, Volcano plots for the DEGs determined by DESeq2 between the main effect of group (MIA versus CON), region (frontal Ctx versus whole Str), and treatment (LPS versus SAL) correcting for the other covariate variables from MACS-isolated CD11b+ cells. Black, q < 0.05. **f**, Heatmap for the gene expression of cell type specific markers for microglia, neurons, astrocytes, oligodendrocytes, and macrophages from FACS-isolated CD45^{low}; CD11b+ cells from the whole Str. **g**, Clustering of bulk microglia RNA sequencing samples from (f). MS6 was removed from subsequent analysis due to low read count. Sample naming is as follows: first position M (MIA, red) or C (CON, black), second position S (saline, blue) or L (LPS, green), and third position is animal number.
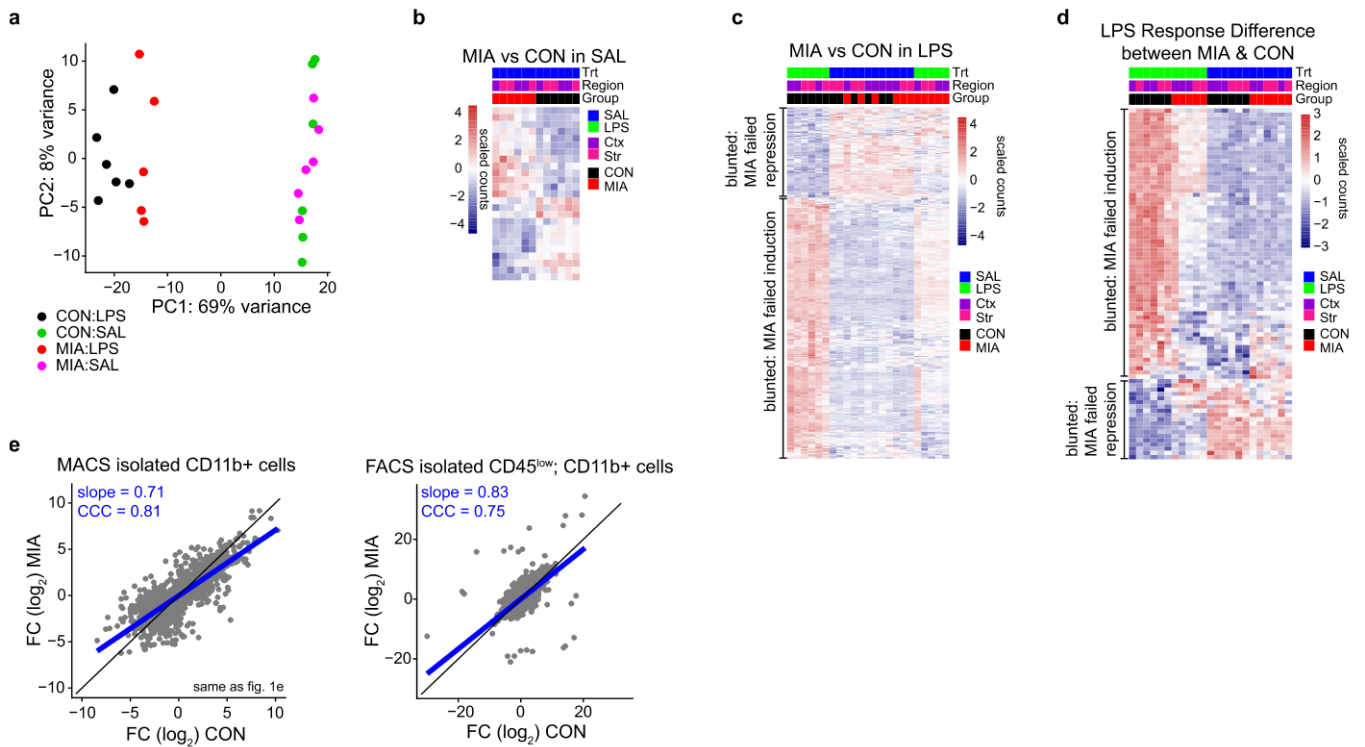
**Extended Data Fig. 2 | PCA and Heatmaps for DEGs represented in Fig. 1. a**, Principal component analysis (PCA) of CON and MIA microglia after SAL or LPS treatment. **b**, Top 25 DEGs between MIA and CON microglia after SAL treatment. **c**, Top DEGs between MIA and CON microglia after LPS treatment. Blunted LPS-induced genes and blunted LPS-repressed genes are indicated. **d**, Top DEGs between MIA and CON microglia that show an interaction between MIA and LPS (group x treatment). Blunted LPS-induced and LPS-repressed genes are indicated. **e**, Linear regression of the FC for the LPS-induced DEGs from Figure 1e of MACS-isolated microglia (left) in comparison with the FACS-isolated microglia (right). The black line indicates the y = x line and the blue line is the linear fit line with slope equal to 0.71 and 0.83, respectively and CCC equal to 0.81 and 0.75, respectively.
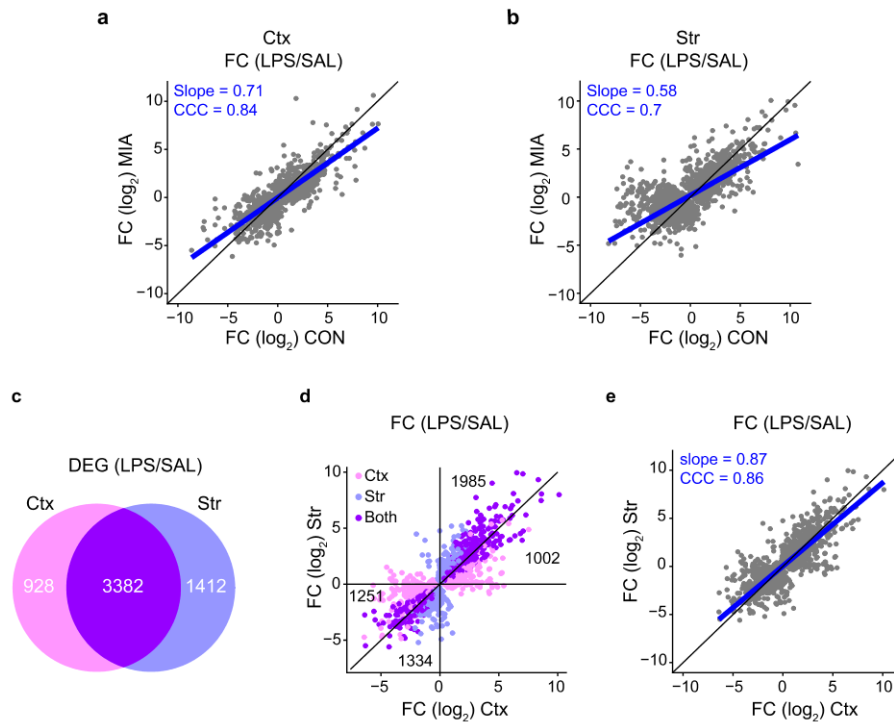
Extended Data Fig. 3 | Regional specificity of the diminished microglia immune response after MIA. a–b, Regional specificity of the MIA blunted LPS response. Linear regression of the FC for the LPS-induced DEGs between microglia from the frontal Ctx (a) or whole Str (b) with slope equal to 0.71 and 0.58, respectively and CCC equal to 0.84 and 0.70, respectively. **c–e**, Control analysis of the LPS responsiveness between microglia from the Ctx compared with microglia from the Str (these are the mixture of both CON and MIA microglia). **c**, Venn diagram of DEGs (q < 0.05) between SAL and LPS in the Ctx microglia (pink) compared with the Str microglia (blue). **d–e**, Plot (d) and linear regression (e) of the FC for the LPS-induced DEGs in both Ctx and Str microglia (purple), only Ctx microglia (pink) or only Str microglia (light blue). Numbers indicate the total number of LPS response genes in each section. The black line indicates the y=x line and the blue line is the linear fit line (slope = 0.87 and CCC = 0.86).
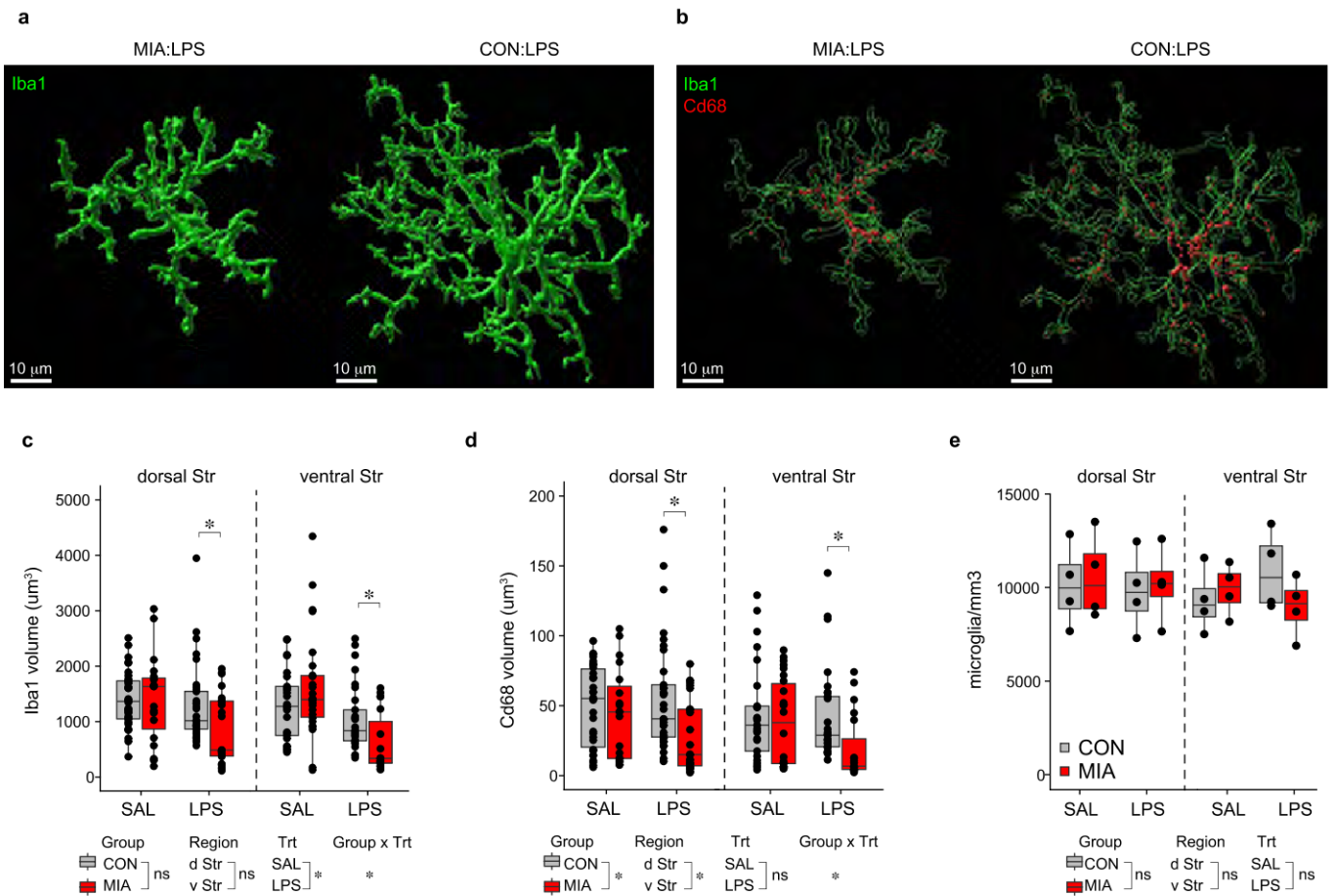
Extended Data Fig. 4 | Microglia density and morphology in the striatum after MIA. a–b, Representative confocal reconstructions of microglia morphology (a) and CD68 lysosomal content (b) in CON and MIA offspring after LPS treatment. Scale bar = 10 μm **c**, Volume of Iba1+ (microglia) in the dorsal and ventral Str of CON (grey) and MIA (red) microglia after SAL and LPS treatment. n are individual cells. Data are analysed by a three-way ANOVA with emmeans post hoc test. $n_{CON:SAL:DS}$=34 cells from 4 mice from 4 litters, $n_{MIA:SAL:DS}$=19 cells from 4 mice from 3 litters, $n_{CON:SAL:VS}$=25 cells from 4 mice from 4 litters, $n_{MIA:SAL:VS}$=26 cells from 4 mice from 3 litters, $n_{CON:LPS:DS}$=33 cells from 4 mice from 4 litters, $n_{MIA:LPS:DS}$=26 cells from 3 mice from 2 litters, $n_{CON:LPS:VS}$=29 cells from 4 mice from 4 litters, $n_{MIA:LPS:VS}$=19 cells from 3 mice from 2 litters. Group: $F_{(1, 206)}$ = 1.7, p = 0.197, Trt: $F_{(1, 206)}$=22, p = 5e-6, Region: $F_{(1, 206)}$ = 1.3, p=0.26, Interaction: $F_{(1, 206)}$ = 10.46, p = 0.0014, emmeans: MIAvCON$_{LPS:DS}$: t(203) = 2.39, p = 0.018, MIAvCON$_{LPS:VS}$: t(203)=2.20, p=0.029, MIAvCON$_{SAL:DS}$: t(203) = −0.06, p = 0.95, MIAvCON$_{SAL:VS}$: t(203) = −1.7, p = 0.10. **d**, Volume of CD68 (lysosomes) inside microglia from the dorsal and ventral Str of CON (grey) and MIA (red) offspring after SAL and LPS treatment. n are individual cells. Data are analysed by a three-way ANOVA with emmeans post hoc test. n same as in c. Group: $F_{(1, 206)}$ = 11.9, p = 6E-4, Trt: $F_{(1, 206)}$ = 1.77, p = 0.185, Region: $F_{(1, 206)}$ = 4.32, p = 0.039, Int: $F_{(1, 206)}$ = 4.44, p = 0.036, emmeans: MIAvCON$_{LPS:DS}$: t(203) = 3.19, p = 0.0017, MIAvCON$_{LPS:VS}$: t(203)=2.34, p = 0.020, MIAvCON$_{SAL:DS}$: t(203)=0.669, p = 0.504, MIAvCON$_{SAL:VS}$: t(203) = 0.727, p = 0.468. **e**, Microglia density in the dorsal and ventral Str of CON (grey) and MIA (red) offspring after SAL or LPS treatment. n are individual animals. Data are analysed by a three-way ANOVA with no significant difference between group, region, or treatment. $n_{CON:SAL}$=4 mice from 4 litters, $n_{CON:LPS}$=4 mice from 4 litters, $n_{MIA:SAL}$=4 mice from 3 litters, $n_{MIA:LPS}$=4 mice from 3 litters. Group: $F_{(1, 28)}$ = 0.036, p = 0.85, Treatment: $F_{(1, 28)}$ = 0.001, p = 0.98, Region: $F_{(1, 28)}$ = 0.363, p = 0.55. The box plots in **c-e** show the median (centre line), the IQR (box limits) and 1.5 × IQR (whiskers). * p < 0.05.

a

b

c

d

e

g

h


f

i

j

k

l

m
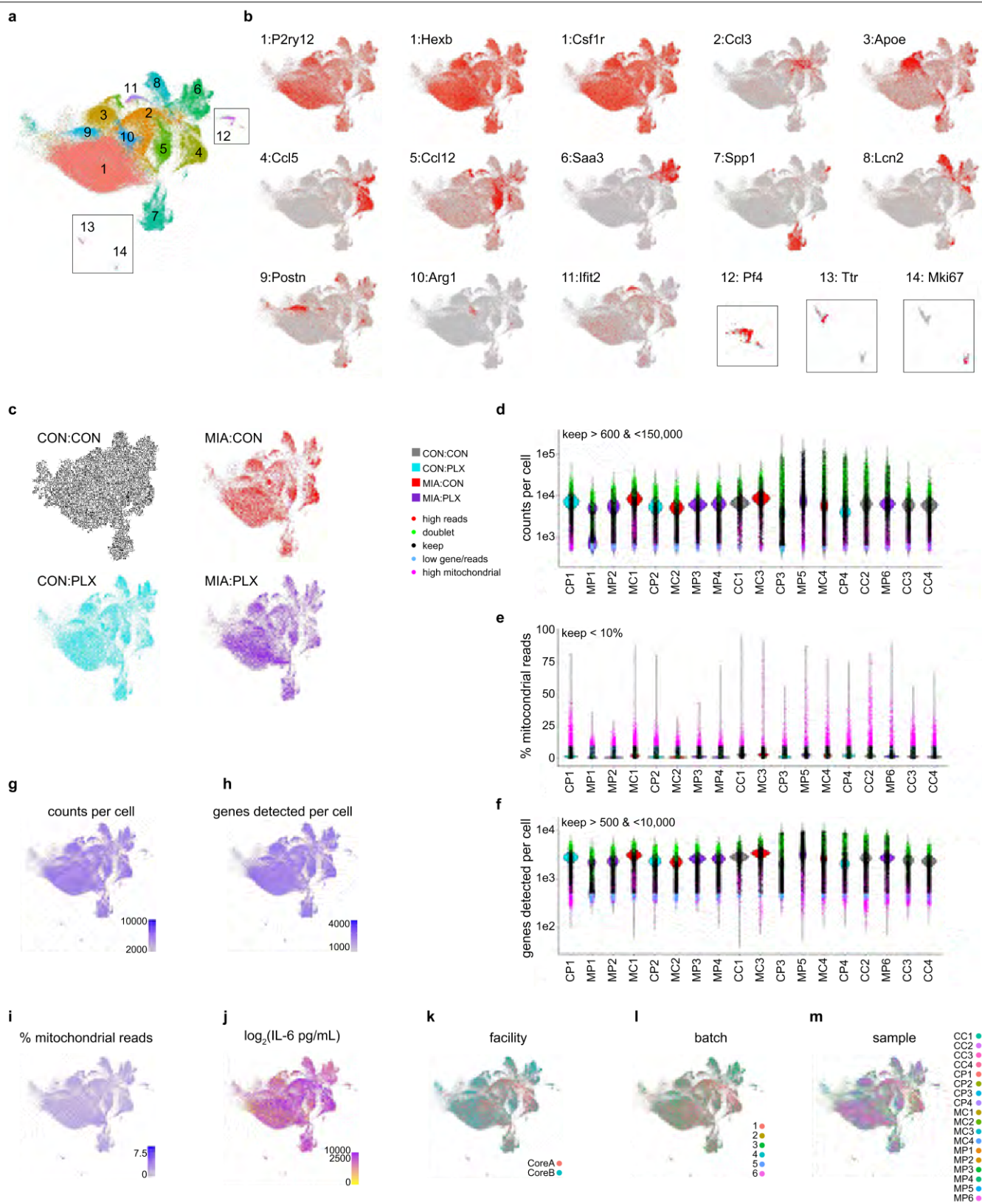
Extended Data Fig. 5 | See next page for caption.

Extended Data Fig. 5 | Single cell RNA sequencing of LPS-activated striatal microglia from CON and MIA offspring with prenatal microglia replacement. a, UMAP of ~120,000 microglia grouped into 14 clusters. Note: 3 clusters were removed due to markers for poor cell quality resulting in 14 high quality cell clusters. **b**, Markers enriched for each cluster. Cluster 1 is homeostatic microglia expressing *P2ry12, Hexb*, and *Csf1r*. Cluster 2 expresses *Ccl3*, cluster 3 expresses *Apoe*, cluster 4 expresses *Ccl5*, cluster 5 expresses *Ccl12*, cluster 6 expresses *Saa3*, cluster 7 expresses *Spp1*, cluster 8 expresses *Lcn2*, cluster 9 expresses *Postn*, cluster 10 expresses *Arg1*, cluster 11 expresses *Ifit2* and *Cxcl10*. Cluster 12 and 13 are macrophage clusters expressing *Pf4* and *Ttr*, respectively. Cluster 14 is a proliferative cluster expressing *Mki67* and *Top2a*. **c**, Clustering distribution of microglia from CON (CON:CON, black), MIA (MIA:CON, red), prenatal microglia replacement (CON:PLX, cyan), and MIA with prenatal microglia replacement (MIA:PLX, purple). **d**–**f**, Filtering of all cells (~147,000) for low counts per cell (d, blue dots < 600 counts), low number of total genes detected per cell (f, blue dots, < 500 genes), high mitochondrial content (e, magenta, > 10% mitochondrial), doublet detection (green dots) or high read count (red dot, > 150,000). **d**, RNA counts per cell for each sample; cells were retained with counts > 600 and < 150,000. **e**, Percent mitochondrial reads per cell for each sample; cells were retained with < 10% mitochondrial content. **f**, Number of genes detected per cell for each sample; cells were retained with > 500 genes and < 10,000 genes detected. Cell doublets were also removed and indicated by green dots in d-f. **g**–**m**, UMAP of cells after filtering. **g**, UMAP of counts per cell. **h**, detected genes per cell. **i**, percent mitochondrial reads per cell. **j**, serum IL-6 expression quantified in each sample. **k**, batch effect for processing facility. **l**, batch effect depending on date of processing. **m**, individual samples processed. n are individual cells.
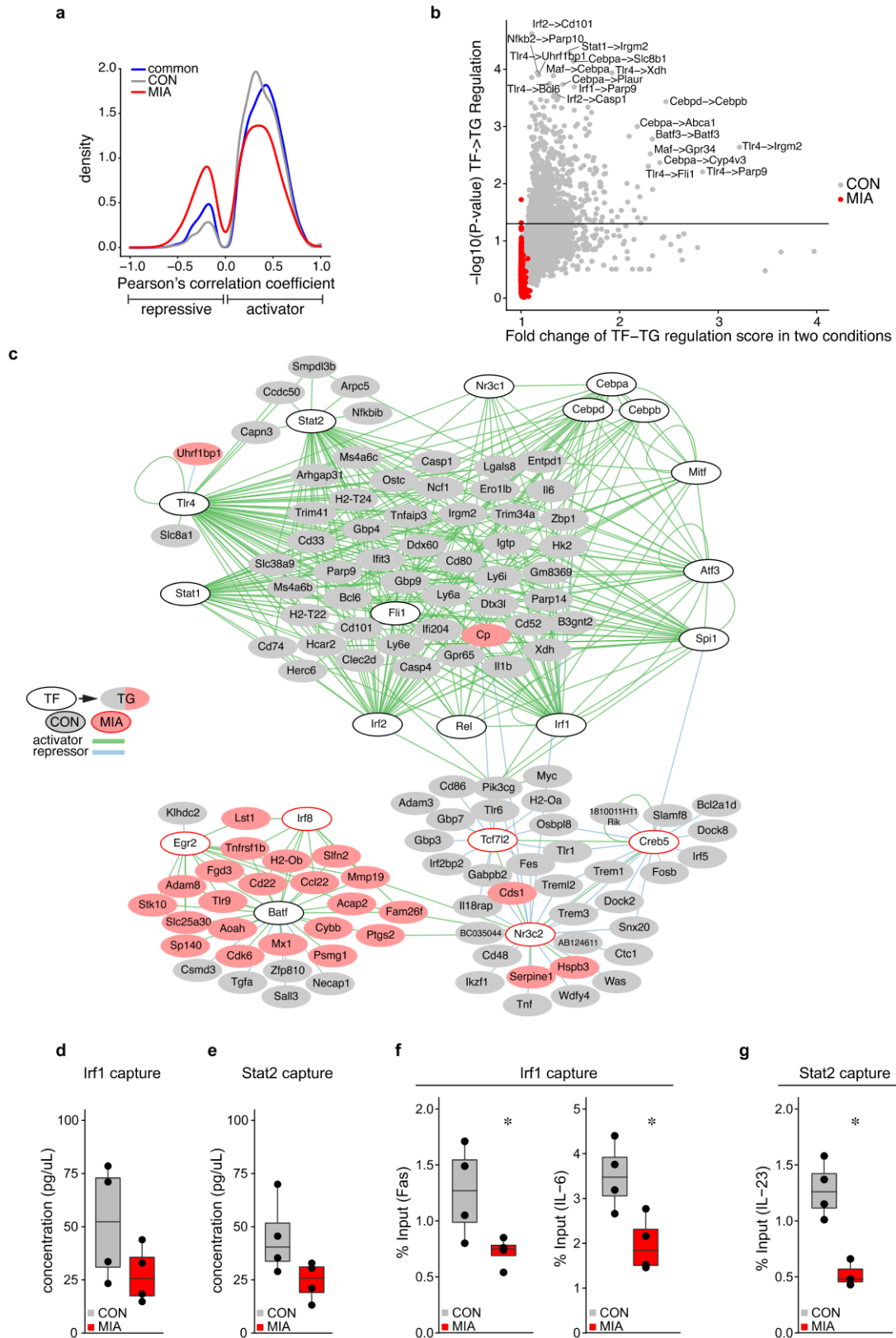
Extended Data Fig. 6 | See next page for caption.

Extended Data Fig. 6 | Network analysis of ATAC and RNA-seq in MIA and CON microglia. a, Density plot of transcription factor (TF) and target (TG) regulation directions predicated from ENCODE data and enriched in MIA and CON microglia. The direction of the regulation was determined using a Pearson's correlation coefficient with negative values indicating a repressive network and positive values indicating an activator network. TF-TG pairs were enriched in the MIA microglia (red), CON microglia (grey) or common in both groups (blue). **b**, Fold change (between MIA and CON) and significance of specific TF-TG pairs in MIA microglia (red) and CON microglia (grey) determined using PECA. **c**, Cytoscape network of the most highly enriched TF-TG networks with colour indicating the enrichment for CON (grey) or MIA (red). The lines indicate the TF-TG network. **d–e**, Total concentration of DNA captured by CUT&RUN with antibodies against IRF1 (d) and STAT2 (e) IRF1: n_{CON}=4 mice from 2 litters, n_{MIA}=4 mice from 2 litters, STAT2: n_{CON}=4 mice from 3 litters, n_{MIA}=4 mice from 2 litters. **f–g**, Specific target DNA captured using CUT&RUN-qPCR represented as percent of total input DNA by the TF IRF2 (f), or STAT2 (g) for target genes of IRF1: *Fas* and *Il-6* and STAT2: *Il-23a*. n are individual animals. Data are analysed by a two-sided t-test. n same as d-e. ITF1-*Fas*: t(6) = 2.5, p = 0.047, IRF1-*Il-6*: t(6)=3.15, p = 0.02, STAT2-*Il-23*: t(5) = 4.74, p = 0.005. The box plots in d–g show the median (centre line), the IQR (box limits) and 1.5 × IQR (whiskers).* p < 0.05.
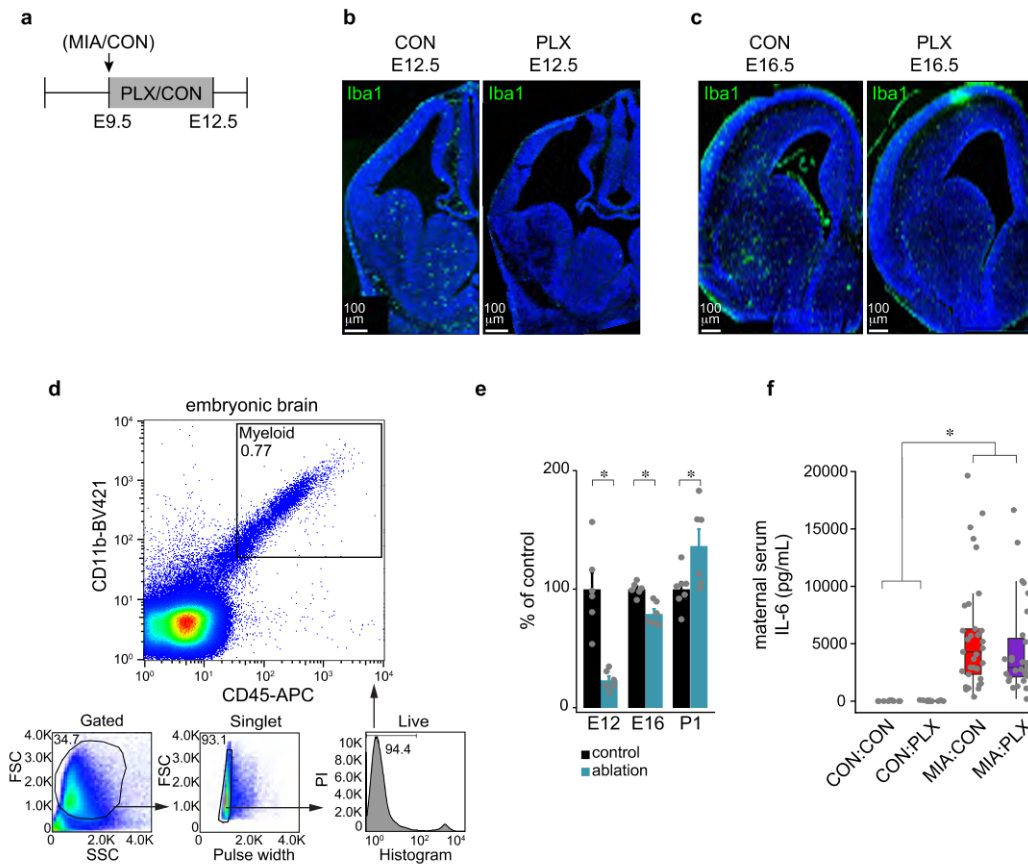
Extended Data Fig. 7 | Ablation and repopulation efficiency of embryonic microglia. a, Timeline of PLX5622 (PLX) treatment. **b**–**c**, Representative images of E12.5 (b) and E16.5 (c) brain slices with high efficiency of ablation after 3 days of ablation treatment (b) and 4 days of repopulation (c). Green= Iba1, Blue=Dapi, scale bar = 100 μm. Images are representative from 4-9 individual animals per condition. **d**, FACS sorting plot for quantification of repopulation of brain myeloid cells after gating for live singlets, the CD11b^{+}, CD45^{+} cells were quantified relative to control animals. FSC=forward scatter, SSC=side scatter, PI=propidium iodide. **e**, Quantification of microglia ablation and re-infiltration. n are individual animals. Data are shown as mean ± s.e.m and analysed using a two-sided t-test. $n_{CON:E12}$=6 mice from 2 litters, $n_{PLX:E12}$ = 6 mice

from 2 litters, $n_{CON:E16}$=6 mice from 1 litter, $n_{PLX:E16}$ = 6 mice from 2 litters, $n_{CON:P1}$ = 7 mice from 3 litters, $n_{PLX:P1}$=6 mice from 2 litters. E12: t(6)=5, p = 0.002, E16: t(8) = 5, p = 0.002, P1: t(7) = −2, p = 0.05. **f**, IL-6 protein expression in maternal serum 3 h after PIC or SAL injection with and without prenatal PLX treatment. n are individual animals. Data are analysed using a two-way ANOVA with Tukey post hoc test. *p < 0.05. $n_{CON:CON}$=27 litters, $n_{CON:PLX}$=24 litters, $n_{MIA:CON}$=33 litters, $n_{MIA:PLX}$=27 litters. Group: $F(3, 91)$=230.7, p < 2e-16, CON:PLX v CON:CON: t(91)=1.5, p=0.343, MIA:CON v CON:CON: t(91)=19.9, p < 1e-4, MIA:PLX v CON:CON: t(91)=18.6, p < 1e-4, MIA:PLX v MIA:CON: t(91)=−0.622, p=0.891. The box plots in **f** show the median (centre line), the IQR (box limits) and 1.5 × IQR (whiskers).
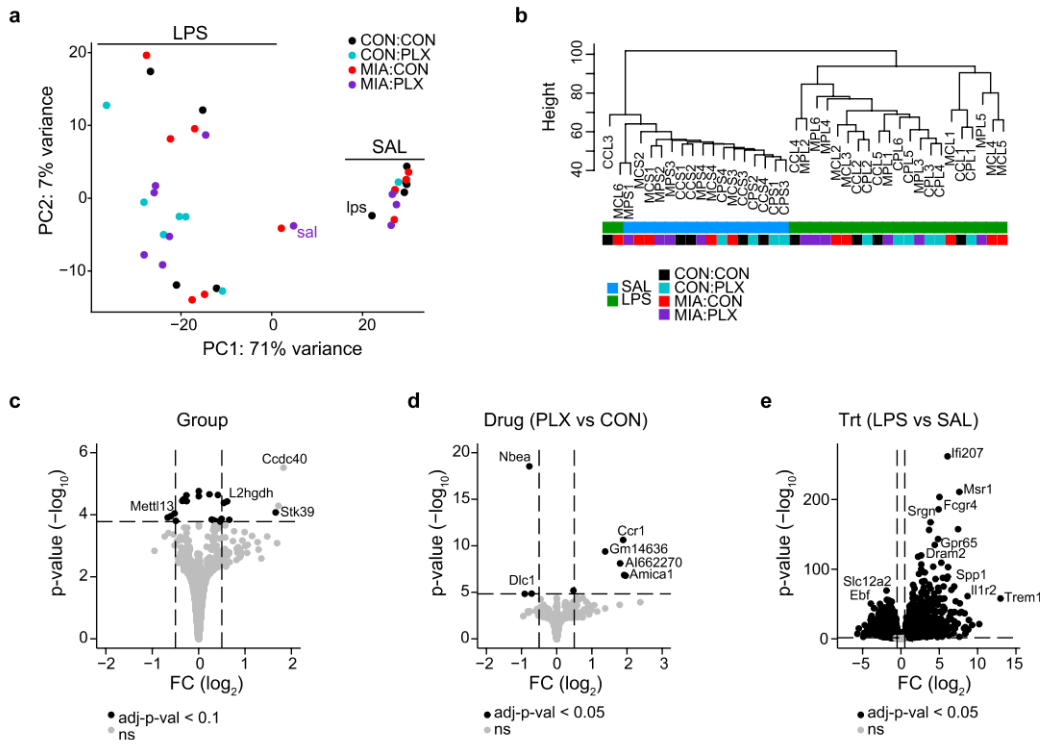
Extended Data Fig. 8 | Rescue of microglia blunting in MIA offspring using prenatal microglia replacement. a, PCA of microglia from CON:CON (black), CON:PLX (cyan), MIA:CON (red), and MIA:PLX (purple) from the whole Str. Two samples were excluded due to incorrect clustering, each labelled accordingly. **b**, Clustering of bulk microglia RNA sequencing samples from (a). **c**–**e**, Volcano plots for the DEGs between the main effect of group (c, among CON:CON, CON:PLX, MIA:CON, and MIA:PLX), PLX treatment (d, PLX versus CON), and LPS treatment (e, SAL versus LPS) correcting for the other covariate variables. Black = q < 0.05 using DESeq2.
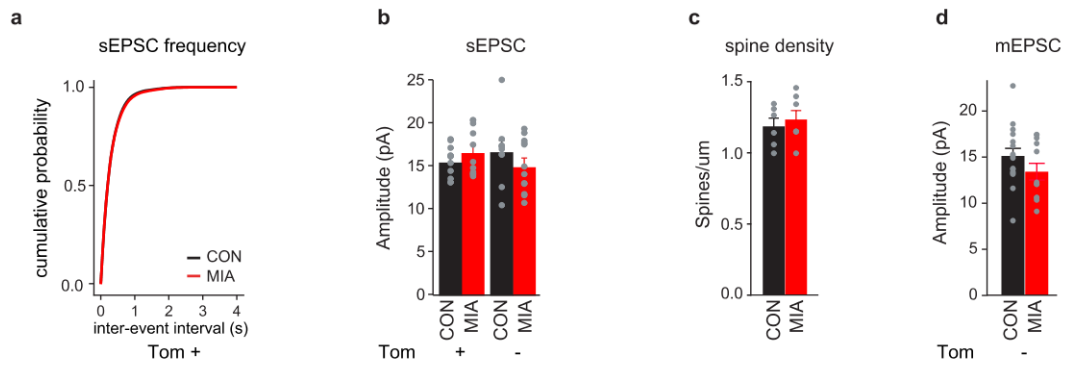
Extended Data Fig. 9 | Rescue of neuronal electrophysiological phenotypes in MIA offspring using prenatal microglia replacement related to Fig. 5. **a**, Two-sample KS test for the cumulative distribution of the inter-event intervals of the sEPSC frequency from Tom+ (D1R) in Fig. 5c. $n_{Con:D1R}$=11 cells from 8 animals from 5 litters, $n_{MIA:D1R}$=10 cells from 4 animals from 3 litters. **b**, sEPSC amplitude of Tom+ (D1R) and Tom- (D2R) medium spiny neurons (MSNs) in Fig. 5c. n are individual cells. Data are shown as mean ± s.e.m and analysed using t-tests. $n_{CON:D1R}$=11 cells from 8 animals from 5 litters, $n_{MIA:D1R}$=10 cells from 4 animals from 3 litters, $n_{CON:D2R}$ = 10 cells from 6 animals from 4 litters, $n_{MIA:D2R}$=13 cells from 6 animals from 4 litters. **c**, Spine density of striatal MSNs in the ventral Str. n are individual animals. Data are shown as mean ± s.e.m and analysed using a t-test. n_{Con} = 6, mice from 3 litters from 28 cells, n_{MIA} = 7 mice from 3 litters from 34 cells. **d**, mESPC amplitudes of Tom- (D2R) MSNs analysed in Fig. 5e. n are individual cells. Data are shown as mean ± s.e.m and analysed using a t-test. $n_{CON:D2R}$=16 cells from 3 animals from 2 litters, $n_{MIA:D2R}$=12 cells from 3 animals from 2 litters..
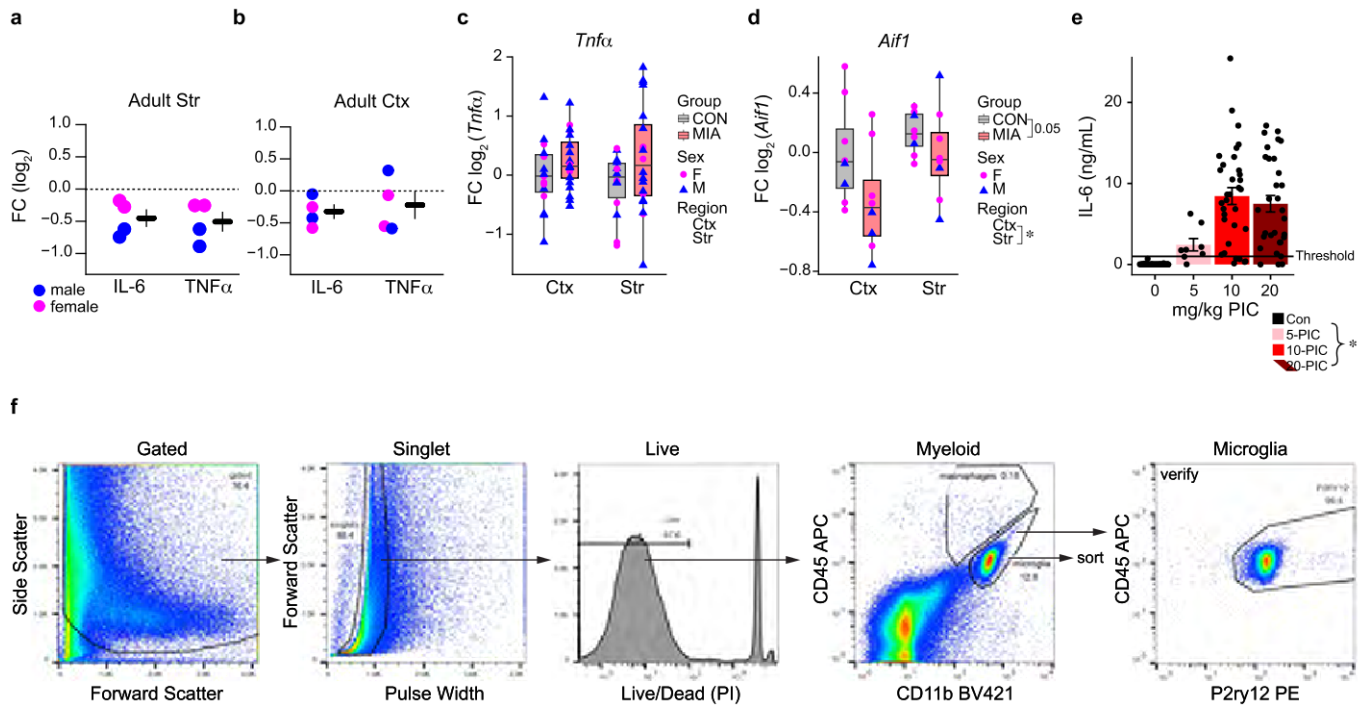
Extended Data Fig. 10 | Sex effect in MIA and three-hour dose response in maternal serum after MIA. a–b, Quantification of secreted IL-6 and TNFα from LPS-stimulated microglia *in vitro* at adulthood from the Str (a) and frontal Ctx (b) from Fig. 2a-b indicating the sex [male (blue) and female (pink)] of each offspring. n are independent culture experiments. Data are shown as mean ± s.e.m. with each experiment normalized to CON. Adult: $n_{All groups}$ = 4 cultures each with 2 mice pooled from 3 litters for both CON and MIA. **c–d**, Baseline gene expression analysed by qPCR for *Tnfα* (c) and *Aif1* (d) from bulk frontal Ctx and whole Str from CON (grey) and MIA (red) offspring indicating the sex [male (blue) and female (pink)] of each animal. n are individual animals. Data are shown as median ± IQR range with 1.5*IQR whiskers and analysed by a linear mixed-effect modelling and three-way ANOVA. *Tnfα*: $n_{CON:CTX:female}$ = 6 mice from 4 litters, $n_{CON:CTX:male}$ = 9 mice from 7 litters, $n_{CON:STR:female}$ = 6 mice from 4 litters, $n_{CON:STR:male}$ = 8 mice from 6 litters, $n_{MIA:CTX:female}$ = 5 mice from 4 litters, $n_{MIA:CTX:male}$ = 15 mice from 9 litters, $n_{MIA:STR:female}$ = 5 mice from 4 litters,

$n_{MIA:STR:male}$ = 15 mice from 9 litters. Group: F(1, 65) = 3.78, p = 0.057, Region: F(1, 65) = 0.042, p = 0.84, Sex: F(1, 65) = 0.43, p = 0.51. *Aif1*: $n_{CON:CTX:female}$ = 6 mice from 4 litters, $n_{CON:CTX:male}$ = 2 mice from 2 litters, $n_{CON:STR:female}$ = 6 mice from 4 litters, $n_{CON:STR:male}$ = 2 mice from 2 litters, $n_{MIA:CTX:female}$ = 5 mice from 4 litters, $n_{MIA:CTX:male}$ = 3 mice from 2 litters, $n_{MIA:STR:female}$ = 5 mice from 4 litters, $n_{MIA:STR:male}$ = 3 mice from 2 litters. Group: F(1, 28) = 4.2, p=0.050, Region: F(1, 28) = 4.5, p=0.043, Sex: F(1, 28) = 1.5, p = 0.23. **e**, IL-6 protein expression in maternal serum 3 h after PIC injection. n are individual animals. Data are shown as mean ± s.e.m and analysed using a two-way ANOVA with Tukey posthoc test. *p < 0.05. $n_{dose:0}$ = 81 litters, $n_{dose:5}$ = 8 litters, $n_{dose:10}$= 62 litters, $n_{dose:20}$ = 28 litters. Group: F(3,162)=45.17, p < 2e-16, 0 v 5: t(162) = 1.7, p = 0.32, 0 v 10: t(162) = 9.8, p < 0.001, 0 v 20: t(162) = 9.4, p < 0.001, 10 v 20: t(162) = 1.7, p = 0.30. Offspring from dams with a serum response below 1,000 pg ml⁻¹ were excluded from subsequent experiments. **f.** The gating strategy for FACS-isolated microglia used in Figs. 1j,k, 3 and 4a–j and Extended Data Figs. 2e, 5, 6 and 8.

Corresponding author(s):   Akira Sawa

Last updated by author(s):   Jul 11, 2022

Reporting Summary

Nature Portfolio wishes to improve the reproducibility of the work that we publish. This form provides structure for consistency and transparency in reporting. For further information on Nature Portfolio policies, see our Editorial Policies and the Editorial Policy Checklist.

Statistics

For all statistical analyses, confirm that the following items are present in the figure legend, table legend, main text, or Methods section.

n/a	Confirmed	
☐	☒	The exact sample size (*n*) for each experimental group/condition, given as a discrete number and unit of measurement
☐	☒	A statement on whether measurements were taken from distinct samples or whether the same sample was measured repeatedly
☐	☒	The statistical test(s) used AND whether they are one- or two-sided *Only common tests should be described solely by name; describe more complex techniques in the Methods section.*
☐	☒	A description of all covariates tested
☐	☒	A description of any assumptions or corrections, such as tests of normality and adjustment for multiple comparisons
☐	☒	A full description of the statistical parameters including central tendency (e.g. means) or other basic estimates (e.g. regression coefficient) AND variation (e.g. standard deviation) or associated estimates of uncertainty (e.g. confidence intervals)
☐	☒	For null hypothesis testing, the test statistic (e.g. F, t, r) with confidence intervals, effect sizes, degrees of freedom and P value noted *Give P values as exact values whenever suitable.*
☒	☐	For Bayesian analysis, information on the choice of priors and Markov chain Monte Carlo settings
☐	☒	For hierarchical and complex designs, identification of the appropriate level for tests and full reporting of outcomes
☐	☒	Estimates of effect sizes (e.g. Cohen's *d*, Pearson's *r*), indicating how they were calculated

Our web collection on statistics for biologists contains articles on many of the points above.

Software and code

Policy information about availability of computer code

Data collection	Adobe Photoshop version CS6, Flow Jo 10.2, Neurolucida Version 2019, Imaris (x64 version 9.5.1), ZEN imaging software.
Data analysis	For all analyses, codes are available on github (https://github.com/lindsaynhayes/Hayes_2022) including packages and versions for each analysis. R 4.0 was the primary data analysis software.

For manuscripts utilizing custom algorithms or software that are central to the research but not yet described in published literature, software must be made available to editors and reviewers. We strongly encourage code deposition in a community repository (e.g. GitHub). See the Nature Portfolio guidelines for submitting code & software for further information.

Data

Policy information about availability of data

All manuscripts must include a data availability statement. This statement should provide the following information, where applicable:
- Accession codes, unique identifiers, or web links for publicly available datasets
- A description of any restrictions on data availability
- For clinical datasets or third party data, please ensure that the statement adheres to our policy

Datasets generated during the current study are available online. All genomics data are available at the NCBI Gene Expression Omnibus under SuperSeries accession number GSE201817. Publicly available databases used in this manuscript include HOCOMOCO v11 (https://hocomoco11.autosome.org) and PECA v2.0. (https://github.com/SUwonglab/PECA). The publicly available GWAS database was collected from the NHGRI GWAS catalog (v1.0.2, https://www.ebi.ac.uk/gwas/) and

included genes with a -log10 p-value >8 and an odds ratio >1 for associations with autism, attention deficit hyperactivity disorder, bipolar disorder, depression, and schizophrenia.

Human research participants

Policy information about studies involving human research participants and Sex and Gender in Research.

Reporting on sex and gender	No human subjects were used in this study.
Population characteristics	No human subjects were used in this study.
Recruitment	No human subjects were used in this study.
Ethics oversight	No human subjects were used in this study.

Note that full information on the approval of the study protocol must also be provided in the manuscript.

Field-specific reporting

Please select the one below that is the best fit for your research. If you are not sure, read the appropriate sections before making your selection.

☒ Life sciences   ☐ Behavioural & social sciences   ☐ Ecological, evolutionary & environmental sciences

For a reference copy of the document with all sections, see nature.com/documents/nr-reporting-summary-flat.pdf

Life sciences study design

All studies must disclose on these points even when the disclosure is negative.

Sample size	No statistical methods were used to predetermine sample size. We used similar sizes to those in the field using similar methods (Badimon Nature 2020, Thion Cell Reports 2019, Schalbetter Sci Advances 2022) aiming for the minimum number of animals needed to reliably detect the expected effect size with an alpha rate set at 0.05 in a standard powered experiment.
Data exclusions	Outliers were detected and removed based on hclust, principal component analysis, and if the RNA sequencing read depth was too low or too high from the sample mean. These are indicated in the supplemental statistics table and manuscript.
Replication	For each assay multiple biological replicates were performed. The detailed biological replicates are outlined in the figure legends and supplemental statistics table.
Randomization	Virgin females were mated to experienced male breeders and the pregnant dams were then randomly assigned to each group. Each experienced male generated females from both groups to control for paternal lineage.
Blinding	Samples were blinded during data collection and analysis for spine counting and microglia morphology because the observer made subjective judgements during the analysis regarding what is counted. Therefore, the analysis was done by the same observer for all samples and grouping was only revealed after all data was collected. Other assays such as ELISA, qPCR, and RNA sequencing were not blinded because the data is collected simultaneously for all groups and the analysis is set for all samples simultaneously.

Reporting for specific materials, systems and methods

We require information from authors about some types of materials, experimental systems and methods used in many studies. Here, indicate whether each material, system or method listed is relevant to your study. If you are not sure if a list item applies to your research, read the appropriate section before selecting a response.

Materials & experimental systems

n/a	Involved in the study
☐	☒ Antibodies
☒	☐ Eukaryotic cell lines
☒	☐ Palaeontology and archaeology
☐	☒ Animals and other organisms
☒	☐ Clinical data
☒	☐ Dual use research of concern

Methods

n/a	Involved in the study
☒	☐ ChIP-seq
☐	☒ Flow cytometry
☒	☐ MRI-based neuroimaging

Antibodies

Antibodies used	For immunohistochemistry: Rabbit anti-Iba1 Wako cat# 019-19741, Lot = SAG4318, 1:500. Rat anti-Cd68 Biorad cat# MCA1957, batch = 1602, 1:100. Donkey anti-rabbit Alexa 488, 1:500, Thermo (A32790). Donkey anti-mouse Alexa 555, 1:500, Thermo (A31570). For flow cytometry: Fc block Rat anti-mouse CD155/CD32 eBiosciences 16-0161-81 at 1:50, Rat anti-mouse CD45-APC BD Biosciences 561018 clone 30-F11 at 1:100 dilution. Rat anti-mouse CD11b-BV421 BD Biosciences 562605 clone M1/70 at 1:100. Biolegend Rat anti-P2RY12-PE (848003) 1:75. For CUT&RUN DNA capture the following validated antibodies were used: IRF1 & STAT2 (Cell Signaling 8478T & 72604S).
Validation	The Wako Iba1 and Biorad CD68 antibodies are widely used with over 150 citations each (https://www.biocompare.com/Product-Reviews/131003-Anti-Iba-1-Polyclonal-Rabbit-Antibody-from-Wako/) (https://images.bio-rad-antibodies.com/datasheets/datasheet-MCA1957.pdf). The FACS antibody specificity was validated by isotype control staining, comparison with unstained cells, and comparison of single-color stains. Furthermore, we verified our gating strategy with a third microglia specific antibody and show this in Extended Data Figure 10. The CUT&RUN antibodies were validated by running a control IgG antibody and ensuring greater specific antibody pull down than the IgG control.

Animals and other research organisms

Policy information about studies involving animals; ARRIVE guidelines recommended for reporting animal research, and Sex and Gender in Research

Laboratory animals	Animals used include C67BL/6J purchased from Jackson labs (00664) and dopamine receptor D1alpha-TdTomato (Drd1α-TdTomato) mice were kindly shared by Dr. Gul Dolen backcrossed to C57BL/6J mouse line. Male mice were used in most assays. In vitro and QPCR assays included both males and females (Ext Data Figure10). Animals were used at 8-12 weeks for the majority of experiments. Animals aged postnatal day 4 were used in Fig 2, embryonic day 18 for Fig 2 and Ext Data Fig 10, and E12 and E16 for Ext Data Fig 7.
Wild animals	We did not use wild animals.
Reporting on sex	We used male mice in most experiments and Ext Data Figure 10 shows the sex of the assays with both sexes included.
Field-collected samples	We did not use field-collected samples.
Ethics oversight	All animal procedures were approved by the IACUC at Johns Hopkins University.

Note that full information on the approval of the study protocol must also be provided in the manuscript.

Flow Cytometry

Plots

Confirm that:

☒ The axis labels state the marker and fluorochrome used (e.g. CD4-FITC).

☒ The axis scales are clearly visible. Include numbers along axes only for bottom left plot of group (a 'group' is an analysis of identical markers).

☒ All plots are contour plots with outliers or pseudocolor plots.

☒ A numerical value for number of cells or percentage (with statistics) is provided.

Methodology

Sample preparation	Brains used for FACS analysis and cells used for bulk RNA sequences were digested in papain and DNase for 20-30 min at 37C. Cells were filtered, debris removed by a density gradient solution (Miltenyi Debris removal solution), washed and stained with antibodies. See Extended Data Figure 7. Cells sorted for single cell RNA sequencing and CUT&RUN, were mechanically dissociated on ice, filtered, debris removed by a density gradient, washed and then stained with antibodies before sorting. See Extended Data Figure 10f
Instrument	Cells were sorted on a MoFlo XDP or MoFlo Legacy sorter.
Software	Data was analyzed using the FlowJo software (v10.2).
Cell population abundance	In the embryonic sorting the myeloid cells were 0.22% of control and 0.05% of the ablated gated cells at E12.5. At E16.5 myeloid cells were 0.72% of control and 0.57% of ablated gated cells. At P1 myeloid cells were 2.7% of control and 3.7% of ablated gated cells. In the single cell and bulk RNA sequencing cell identity was confirmed by expression of known microglia marker genes. See Extended Data Figure 7.
Gating strategy	Cells were gated on forward and side scatter for size selection and on pulse width to get singlets. Live cells were selected by negative propidium iodide staining. Finally the selected cell population was gated based on CD45 and CD11b expression.

☒ Tick this box to confirm that a figure exemplifying the gating strategy is provided in the Supplementary Information.